The Multiple Metamorphism of Mafic Granulites From the East Hebei Terrane, North China Craton: Insights Into the Transition of Tectonic Regimes

Ting Liu[1,2]*, Chunjing Wei[2], Chuan Yang[3]* and Zhuang Li[4]

[1]College of Earth Sciences, Chengdu University of Technology, Chengdu, China, [2]MOE Key Laboratory of Orogenic Belts and Crustal Evolution, School of Earth and Space Sciences, Peking University, Beijing, China, [3]China Transport Telecommunications and Information Center, Beijing, China, [4]College of Geosciences, China University of Petroleum (Beijing), Beijing, China

The East Hebei terrane from the North China Craton preserves the dome–and–keel structures, which was transected by a later linear belt in the north margin. Mafic granulites from the linear belt and domes record two groups of metamorphic ages at Neoarchean and Paleoproterozoic, but their accurate metamorphic peak conditions and paths have not been well addressed. Three samples of mafic granulites, including two-pyroxene granulite (JD15120), garnet-bearing two-pyroxene granulite (YC8-43), and garnet clinopyroxene granulite (JD1546), were documented for detailed metamorphic studies. Two-episode metamorphism can be recognized. The first-episode recovered from JD15120 and YC8-43 is represented by peak assemblage of medium-grained clinopyroxene, orthopyroxene, amphibole, plagioclase, and ilmenite, which yields ultrahigh temperature (UHT) conditions of 940–960°C at 7.5–8.5 kbar and 950–990°C at 8 kbar, respectively, constrained by contours of the maximum anorthite (X_{An}) in plagioclase cores. The post-peak evolution is dominated by cooling with decompression, constrained mostly from the measured core-to-rim decreasing X_{An} in plagioclase. By contrast, the second-episode overprinting is recognized in all samples, but exhibits varying textures. In garnet-bearing samples (YC8-43 and JD1546), the overprinting assemblages are characterized by poikilitic garnet that occurs either as coronae around the first-episode pyroxenes, forming "red-eye socket" textures, or as grains in equilibrium with tiny-grained clinopyroxene, plagioclase, amphibole, rutile, and quartz, forming high-pressure (HP) granulite assemblages. These HP granulite assemblages show peak conditions of ~12 kbar/860°C and ~12.6 kbar/835°C, constrained by contours of the maximum grossular (X_{Grs}) in garnet cores and the minimum X_{An} in plagioclase cores. The post-peak evolution is dominated by isothermal decompression, constrained from the outward decreasing X_{Grs} in garnet and increasing X_{An} in plagioclase. LA-ICP-MS U-Pb zircon dating on JD15120 and JD1546 suggests two metamorphic ages of ~2.49 Ga and ~1.78 Ga, being considered to be correlated with the UHT and HP granulite metamorphism, respectively. Tectonically, the late Neoarchean UHT granulite metamorphism may correlate a vertical sagduction regime, whereas the late

Paleoproterozoic HP granulite metamorphism is favored to register the continental collision in the northern margin of the North China Craton. This study may have indications for the Neoarchean–Paleoproterozoic tectonic transition of the craton.

1 INTRODUCTION

As a window into the lower continental crust, granulites normally record pressure–temperature (P–T) conditions and P–T paths being indicative to tectonic models (Harley 1989, Harley 1998). Their secular change in apparent thermal gradients is also suggestive for revealing different heat flow and rheology in distinct tectonics (Brown and Johnson 2018). In the Archean terranes, almost half of the granulites are ultrahigh temperature (UHT) type with high dT/dP of >22°C/km (Brown 2007; Brown and Johnson 2018), representing extreme thermal conditions related to the coupling between crust, sub-crustal lithosphere, and asthenospheric mantle on a regional scale (Harley 2004; Harley 2008; Kelsey and Hand 2015), whereas the high-pressure (HP) granulites with intermediate dT/dP of 22–11°C/km became dominant after the Archean Eon (Brown and Johnson 2018), being normally considered as the sign for subduction or collision processes in plate tectonics (O'Brien and Rötzler 2003).

Archean cratons, although featured with thick and depleted lithospheric mantle and relatively stable from subsequent tectonism (Jordan 1978), can have transformation of the cratonic structures and development of multiple metamorphism in response to later reworking events (e.g., Weber 1984; Mahan et al., 2008; Perchuk et al., 2008). For example, the Pikwitonei granulite domain in the Superior Craton, one of the largest Neoarchean high-grade terranes worldwide, was recovered to have undergone multiple metamorphism, involving normal UHT granulite-facies metamorphism with an anticlockwise P–T path at Neoarchean, and overprinting greenschist to amphibolite-facies metamorphism with local migmatization at Hudsonian. These distinct metamorphic processes suggest different tectonic settings involving magmatic underplating (Mezger et al., 1990) or overthrusting during crustal thickening (Arima and Barnett 1984) for the first-episode metamorphism, and collision between the Superior Craton and the Churchill Province to form the Thompson belt for the second-episode metamorphism (Weber 1984). Therefore, detailed metamorphic studies on Archean cratons can give insights into the tectonic evolution of the early Earth.
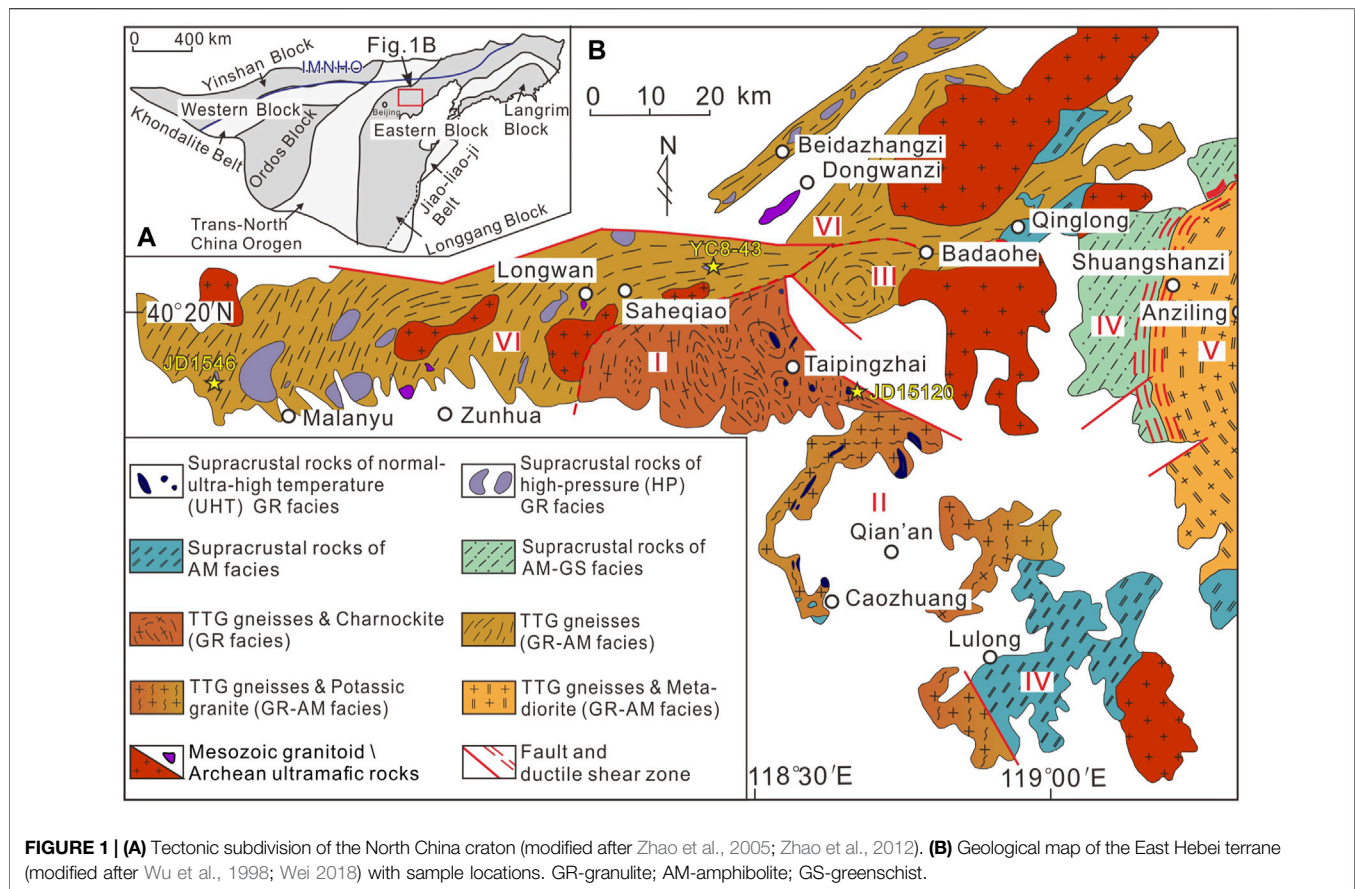
The North China Craton (NCC) consists of four Archean blocks including Ordos, Yinshan, Longgang, and Langrim blocks, and three Paleoproterozoic orogenic belts among them (Zhao et al., 2005). These Archean blocks were revealed to record Neoarchean granulite-facies metamorphism with anticlockwise P–T paths, featured with "red-eye socket" texture in mafic granulites (Zhao et al., 1999; Zhao et al., 2005; Kwan et al., 2016). However, recent studies on mafic granulites from the East Hebei terrane, part of the Longgang block, suggest that some

Archean terranes may be subjected to two episodes of granulite-facies metamorphism at late Neoarchean (2.53–2.47 Ga) and late Paleoproterozoic (1.85–1.80 Ga), respectively (Duan et al., 2015; Yang and Wei 2017b; Lu and Wei 2020). The first-episode Neoarchean granulite-facies metamorphism is featured with two-pyroxene granulites, and is argued to have peak conditions of normal UHT granulite facies of 8.0–11.0 kbar/756–940°C using conventional geothermobarometers (He and Ye 1992; Chen and Li 1996; Zhao et al., 1999; Kwan et al., 2016; Yang and Wei 2017a), or 9.0–10.0 kbar/950–1,070°C using rare earth elements (REE)-based geothermometers (Yang and Wei 2017a). On account of that conventional Fe–Mg exchange geothermometers are more likely to record lower temperatures than the peak of granulites as a result of the fast diffusion during cooling (e.g., Frost and Chacko 1989; Pattison et al., 2003), and the REE-based geothermobarometers generally have large uncertainties (Yang and Wei 2017a), the peak conditions for the two-pyroxene granulites remain uncertain. The second-episode Paleoproterozoic metamorphism was first recognized in mafic dykes, characterized by HP granulite-facies assemblages, which record P–T conditions of 11–12 kbar/790–810°C with clockwise P–T paths at ~1.82 Ga (Duan et al., 2015). Similar overprinting assemblages were also observed in Neoarchean mafic granulites, which exhibit peak P–T conditions of 12.5–12.8 kbar/880–900°C, metamorphic zircon ages of 1.83–1.81 Ga, and garnet-whole rock Lu–Hf isochron ages of 1.77–1.79 Ga (Yang and Wei 2017a; Yang and Wei 2017b; Lu and Wei 2020). However, Wang et al. (2018) argued that the HP granulite metamorphism may have occurred at early Paleoproterozoic (~2.46 Ga), which was followed by heating and decompression to form two-pyroxene granulites. Thus, detailed petrological and geochronological studies on both two-pyroxene and HP granulites need to be further conducted to document their metamorphic evolution.

In this article, representative mafic granulites that have been studied using major element- and REE-based geothermobarometers in Yang and Wei (2017a), were selected for constraining their metamorphic P–T conditions and paths on the basis of the pseudosections calculated using THERMOCALC. Zircon U–Pb dating was also carried out for defining the metamorphic ages.

2 GEOLOGICAL SETTING

The NCC can be normally divided into Eastern and Western Blocks (e.g., Zhao et al., 1998; Zhao et al., 2005; Zhao et al., 2012; **Figure 1A**). It is suggested that the Western Block formed at ~1.95 Ga by the collision between the Yinshan and Ordos Blocks

FIGURE 1 | (A) Tectonic subdivision of the North China craton (modified after Zhao et al., 2005; Zhao et al., 2012). **(B)** Geological map of the East Hebei terrane (modified after Wu et al., 1998; Wei 2018) with sample locations. GR-granulite; AM-amphibolite; GS-greenschist.

along the Khondalite Belt, whereas the Eastern Block formed at ~1.90 Ga when the Longgang and Langrim blocks collided along the Jiao–Liao–Ji Belt (e.g., Zhao et al., 1998; Zhao et al., 2005; Zhao et al., 2012). The time of the final amalgamation between Western and Eastern Blocks along the Trans-North China Orogen (TNCO) is controversial: one view suggests that it occurred at ~1.85 Ga (Zhao et al., 1998; Zhao et al., 2005; Zhao et al., 2012), whereas another view favors an older collision age of ~1.95 Ga (Qian et al., 2013; Qian et al., 2015; Qian and Wei 2016), and interprets the age of ~1.85 Ga to represent a separated orogenic event occurred along the northern margin of the NCC (Wei 2018; Qian et al., 2019). In addition, accretionary and collisional tectonics were also proposed for the NCC, including 2.6–2.5 Ga Atlantic-type passive margin on the western side of the Eastern Block, the ~2.5 Ga collision between the arc/accretionary prism and the Eastern Block, ~2.43 Ga amalgamation of Western Block and Eastern Block along the Central Orogenic Belt (COB, approximate TNCO), and the 2.3–1.9 Ga collision along the Inner Mongolia-North Hebei Orogenic Belt (IMNHO) at the north margin of the NCC (Kusky et al., 2016).

The early Precambrian East Hebei terrane, located in the northwestern of the Longgang Block, can be divided into six litho–tectonic units (**Figure 1B**) including the Taipingzhai ovoid-structural domain (I), Qian'an gneiss dome (II), Badaohe gneiss dome (III), Lulong–Shuangshanzi supracrustal belt (IV), Anziling

gneiss dome (V) and Saheqiao linear-structural belt (VI), following Wu et al. (1998) and Wei (2018). There is near-vertical normal shear in the Shuangshanzi shear zone between the Anziling dome and the Lulong–Shuangshanzi supracrustal belt formed due to the upwelling of the dome with respect to the down-slipping of the belt (Liu et al., 2017; Zhao et al., 2021). Therefore, the terrane well preserves Archean unique dome–and–keel structure although later deformation marked by numerous NE-to NEE-striking shear zones in the Saheqiao linear-structural belt occurred (Liu and Yang 1994; Kusky et al., 2016; Zhao et al., 2021). As show at **Figure 1B**, the East Hebei terrane mainly consists of Neoarchean TTG gneisses, charnockites, potassic granites, and supracrustal rocks. The TTG gneisses and charnockites show magmatic ages of mostly 2.56–2.48 Ga with a peak at ~2.52 Ga (Liu et al., 1990; Wu and Geng 1991; Geng et al., 2006; Yang et al., 2008; Nutman et al., 2011; Guo et al., 2013; Bai et al., 2014; Bai et al., 2015; Yang et al., 2016a; Yang et al., 2016b), except for a few intrusions in the western margin of Qian'an gneiss dome that have older ages of 3.28–2.94 Ma (Nutman et al., 2011; Sun et al., 2016). They were subjected to amphibolite-to granulite-facies metamorphism at 2.53–2.47 Ga (Geng et al., 2006; Yang et al., 2008; Nutman et al., 2011; Bai et al., 2014; Bai et al., 2015). The supracrustal rocks, mainly comprising metasedimentary and metabasic rocks with a few banded iron formation and ultramafic interlayers (Geng et al., 2006; Polat et al., 2006), commonly occur as rafts within or as

FIGURE 2 | Field occurrence of mafic granulites. **(A,B)** Mafic granulites occurring as rafts or enclaves with clear or blurry boundaries within TTG rocks. **(C)** Mafic granulites with penetrative foliation. **(D)** Heterogeneous mafic granulites with diverse distributions of leucosomes.

belts between TTG gneiss domes (Wei 2018). Most of the metasedimentary rocks share similar protolith deposition ages of 2.53–2.50 Ga (Wan et al., 2015; Sun et al., 2016; Duan et al., 2017; Lu et al., 2017; Liu and Wei 2020), except for fuchsite-bearing quartzite that outcropped at Caozhuang and Luanxian areas having deposition age of >3.5 Ga (Liu et al., 1990; Nutman et al., 2011; Chu et al., 2016). The metabasic rocks were mostly dated to have protolith magmatic ages of 2.61–2.52 Ga with a few at ~2.90 Ga (Zhang et al., 2012; Guo et al., 2013; Fu et al., 2016; Liou et al., 2017). Ultramafic rocks, mostly including serpentinized peridotite, picritic amphibolites, and pyroxenite, are argued to be komatiites (Zhang et al., 1980), intra-oceanic suprasubduction zone ophiolitic rocks (Polat et al., 2006), or remnants of an enriched mantle plume (Wang et al., 2019). These supracrustal rocks were normally dated to have two groups of metamorphic ages at 2.53–2.47 Ga and 1.85–1.80 Ga as have mentioned in introduction (e.g., Yang and Wei 2017b; Lu and Wei 2020). The former episode of metamorphism is widely recorded in the whole East Hebei terrane, corresponding to amphibolite-to greenschist-facies metamorphic conditions in Lulong–Shuangshanzi supracrustal belt (Qi et al., 1999; Guo et al., 2013), amphibolite-facies condition of 10–11 kbar/780–800°C with clockwise $P–T$ path in the Caozhuang area (Liu et al., 2020), and the granulite-facies (9.6–10.3 kbar/860–900°C) to UHT (9–10 kbar/>1,000°C) peak conditions with anticlockwise $P–T$ paths in the western margin of Qian'an gneiss dome, Taipingzhai ovoid-structural domain and Saheqiao linear-structural belt (Kwan et al., 2016; Yang

and Wei 2017a; Duan et al., 2017; Lu et al., 2017; Liu and Wei 2018; Lu and Wei 2020; Liu et al., 2021). By contrast, the second-episode metamorphism is locally recognized in the northern part of the terrane, mostly in the Saheqiao linear-structural belt and the Taipingzhai ovoid-structural domain, and dominated by HP granulite-facies metamorphism as have been mentioned in introduction (Duan et al., 2017; Yang and Wei 2017a; Lu and Wei 2020). In addition, there are mafic dykes crosscutting the foliation of Archean TTG gneisses and supracrustal rocks in the Saheqiao linear-structural belt and the Taipingzhai ovoid-structural domain (Chen 1990; Song 1990), and proposed to have experienced HP granulite-facies metamorphism in the later overprinting metamorphism (Duan et al., 2015).

In this study, mafic granulites were collected from the Malanyu, Saheqiao, and Taipingzhai areas. The sample locations are shown on **Figure 1B**. These granulites occur as rafts with clear or blurry boundaries within TTG rocks (**Figures 2A,B**). Most of them have weak or penetrative foliations (**Figure 2C**) and are heterogeneous with the diverse distributions of leucosomes (**Figure 2D**).

3 PETROLOGICAL ANALYSES

3.1 Bulk-Rock Compositions

Among the selected samples, two-pyroxene granulite (JD15120) was collected from the Taipingzhai ovoid-structural domain,

TABLE 1 | Bulk-rock compositions of samples in this study.

Sample	Type	ICP-OES whole rock composition (wt%)										
		SiO$_2$	TiO$_2$	Al$_2$O$_3$	TFe$_2$O$_3$	MnO	MgO	CaO	Na$_2$O	K$_2$O	P$_2$O$_5$	LOI
JD15120	Two-pyroxene granulite	48.76	0.76	14.06	12.56	0.20	7.90	10.68	2.88	0.90	0.11	0.47
YC8-43	Garnet two-pyroxene granulite	47.74	0.92	13.41	14.14	0.23	7.51	12.64	2.05	0.25	0.08	0.22
JD1546	Garnet clinopyroxene granulite	47.41	0.87	12.02	16.01	0.21	6.86	11.60	2.19	0.81	0.14	1.21

		Normalized molar proportions used for phase equilibria modeling (mole %)										
Sample	Figure	H$_2$O	SiO$_2$	Al$_2$O$_3$	CaO	MgO	FeO	K$_2$O	Na$_2$O	TiO$_2$	O	Mg$^\#$
JD15120	**Figure 6A**	2.51	48.65	8.45	10.84	12.16	12.16	0.69	2.79	0.85	0.91	50
YC8-43	**Figure 7A**	0.70	50.36	8.51	13.20	12.05	11.22	0.18	2.10	1.00	0.68	52
YC8-43 (overprinting)	**Figure 7B**	0.95	50.50	7.93	12.11	10.33	14.09	0.20	1.56	0.84	1.48	42
JD1546	**Figure 8**	1.20	50.23	8.14	13.22	11.15	12.84	0.18	1.64	0.70	0.70	46

Wt%, major element oxides in weight percent; LOI, loss on ignition; mole %, major element oxides in mole percent; Mg$^\#$ = MgO/(MgO + FeO).

TABLE 2 | Selected microprobe analyses for sample JD15120.

Mineral	Cpx-1	Opx-1	Amp-1	Pl-1-c	Pl-1-r	Cpx-2	Opx-2	Amp-2	Pl-2
SiO$_2$	52.25	51.63	42.13	59.06	60.03	52.19	50.97	41.67	59.05
TiO$_2$	0.08	–	1.59	0.03	0.02	0.14	0.06	1.22	0.04
Al$_2$O$_3$	2.21	1.28	11.81	25.03	24.95	2.02	1.40	12.33	24.55
Cr$_2$O$_3$	–	0.02	0.03	–	–	–	0.03	0.04	–
Fe2O3	0.47	1.15	1.53	0.18	0.40	1.88	0.79	3.57	1.86
FeO	9.75	25.06	12.98	–	–	7.28	25.34	11.74	–
MnO	0.82	2.45	0.23	–	–	0.35	1.22	0.21	–
MgO	12.28	18.77	11.16	–	0.03	13.08	18.99	11.09	0.10
CaO	21.43	0.46	11.52	8.03	7.30	22.65	0.31	10.83	7.10
Na$_2$O	0.56	0.03	1.56	6.71	7.17	0.54	0.04	1.38	6.96
K$_2$O	–	–	1.45	0.31	0.33	0.02	–	1.53	0.29
Total	99.81	100.75	95.84	99.35	100.24	99.97	99.07	95.25	99.95
O	6	6	23	8	8	6	6	23	8
Si	1.963	1.956	6.385	2.655	2.672	1.945	1.956	6.326	2.649
Ti	–	–	0.181	–	–	0.004	0.002	0.139	–
Al	0.098	0.057	2.110	1.327	1.310	0.089	0.063	2.207	1.298
Cr	–	–	0.004	–	–	–	–	0.005	–
Fe^{3+}	0.013	0.033	0.175	0.006	0.013	0.053	0.023	0.408	0.063
Fe^{2+}	0.306	0.794	1.645	–	–	0.227	0.813	1.490	–
Mn	0.026	0.079	0.030	–	–	0.011	0.040	0.027	–
Mg	0.688	1.060	2.521	–	0.002	0.727	1.086	2.509	0.007
Ca	0.863	0.019	1.871	0.387	0.348	0.905	0.013	1.762	0.341
Na	0.041	0.002	0.458	0.585	0.619	0.039	0.003	0.406	0.605
K	0.000	0.000	0.280	0.018	0.019	0.001	0.000	0.296	0.017
X(phase)	0.69	0.57	0.61	0.39	0.35	0.76	0.57	0.63	0.35

X(Cpx) = X(Opx) = X(Amp) = Mg/(Fe^{2+}+Mg); X(Pl) = X$_{An}$ = Ca/(Ca + Na + K); -c, grain core; -r, grain rim. "–" means that the content is below the detection limit. The mineral formulas were calculated with the program AX (Holland; http://www.esc.cam.ac.uk/astaff/holland/ax.html).

while the garnet-bearing two-pyroxene granulite (YC8-43) and clinopyroxene granulite (JD1546) were from the Saheqiao and Malanyu areas, respectively, in the Saheqiao linear-structural belt (**Figure 1B**; Yang and Wei 2017a). Their bulk-rock compositions, being analyzed using a Leeman Prodigy inductively coupled the plasma-optical emission spectroscopy (ICP–OES) system with high-dispersion Echelle optics at China University of Geoscience (Beijing), are presented in **Table 1**. The three samples share similar compositions with SiO$_2$ of 47.41–48.76 wt%, MgO of

6.86–7.90 wt%, total Fe$_2$O$_3$ of 12.56–16.01 wt%, CaO of 10.68–12.64 wt%, and Mg$^\#$ of 46–52.
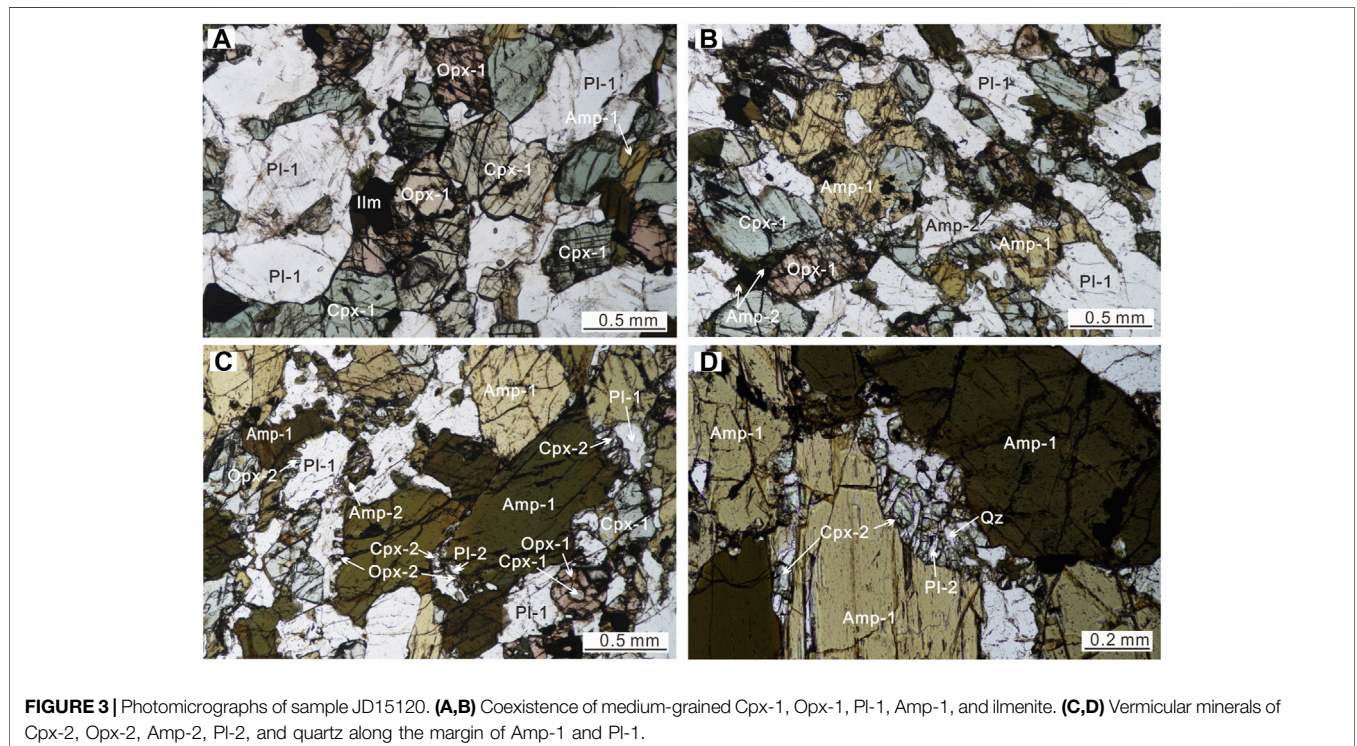
3.2 Petrography and Mineral Compositions

Mineral compositions were analyzed at the Laboratory of Orogenic Belt and Crustal Evolution of Peking University, China, using a JXA-8100 electron microprobe analyzer (EPM; JEOL). The analyses were conducted under operating conditions of 15 KV accelerating voltage and 10 nA probe current with a

TABLE 3 | Selected microprobe analyses for samples YC8-43 and JD1546.

Mineral	YC8-43										JD1546					
	Cpx-1	Opx	Amp	Pl-1-c	Pl-1-r	Cpx-2	Grt-c	Grt-r	Pl-2-c	Pl-2-r	Cpx	Grt-c	Grt-r	Amp	Pl-c	Pl-r
SiO_2	51.01	51.29	41.59	54.31	57.23	52.05	36.83	38.72	61.24	59.09	51.99	38.36	37.69	42.23	61.60	60.03
TiO_2	0.22	0.03	2.29	0.06	–	0.20	–	0.09	0.07	0.05	0.25	0.06	0.10	2.07	–	–
Al_2O_3	3.21	2.33	12.61	29.59	27.46	2.72	20.43	20.09	24.35	25.03	3.63	20.30	20.32	12.42	24.42	25.73
Cr_2O_3	–	0.02	0.03	–	–	0.17	–	0.06	0.04	0.04	0.04	–	–	0.02	0.04	0.03
Fe2O3	2.89	1.75	1.89	0.17	0.14	1.52	4.72	0.84	0.09	0.39	1.71	2.17	3.00	2.10	0.09	0.16
FeO	9.07	23.34	13.32	–	–	8.06	21.02	25.47	–	–	9.67	23.29	23.91	13.50	–	–
MnO	0.26	1.08	0.04	–	–	0.17	1.12	1.23	–	0.05	0.09	1.21	1.26	0.09	0.04	0.03
MgO	12.24	20.26	11.22	–	–	12.34	5.45	5.81	0.02	0.05	11.83	5.11	5.73	11.11	–	–
CaO	20.41	0.56	11.58	12.03	9.58	21.90	9.50	7.22	5.97	6.96	20.82	9.47	7.35	11.47	5.79	7.05
Na_2O	0.84	0.02	1.69	4.64	6.04	0.89	–	–	8.44	7.61	1.05	0.03	0.06	1.61	8.47	7.43
K_2O	0.00	0.00	1.71	0.24	0.27	–	–	0.02	0.25	0.27	–	–	0.02	1.72	0.30	0.21
Total	99.86	100.50	97.78	101.04	100.74	99.87	98.61	99.46	100.47	99.54	100.91	99.79	99.14	98.13	100.77	100.67
O	6	6	23	8	8	6	12	12	8	8	6	12	12	23	8	8
Si	1.913	1.924	6.206	2.430	2.551	1.943	2.909	3.040	2.713	2.654	1.927	3.000	2.968	6.274	2.720	2.658
Ti	0.006	–	0.257	–	–	0.006	–	0.005	0.002	0.002	0.007	0.004	0.006	0.231	–	–
Al	0.142	0.103	2.218	1.561	1.443	0.120	1.902	1.859	1.272	1.325	0.159	1.871	1.886	2.175	1.271	1.343
Cr	–	–	0.004	–	–	0.005	–	0.004	–	–	–	–	–	0.002	–	–
Fe^{3+}	0.081	0.049	0.212	0.006	0.005	0.042	0.279	0.049	0.003	0.013	0.048	0.128	0.178	0.235	0.003	0.005
Fe^{2+}	0.284	0.732	1.662	–	–	0.252	1.389	1.672	–	–	0.300	1.523	1.575	1.677	–	–
Mn	0.008	0.034	0.005	–	–	0.005	0.075	0.082	–	0.002	0.003	0.080	0.084	0.011	–	–
Mg	0.684	1.132	2.495	–	–	0.687	0.641	0.680	0.001	0.003	0.653	0.596	0.672	2.460	–	–
Ca	0.820	0.023	1.852	0.577	0.457	0.876	0.804	0.607	0.283	0.335	0.827	0.793	0.620	1.826	0.274	0.334
Na	0.061	0.002	0.489	0.403	0.522	0.064	–	–	0.725	0.663	0.075	0.005	0.009	0.464	0.725	0.638
K	0.000	0.000	0.326	0.014	0.015	–	–	0.002	0.014	0.015	–	–	0.002	0.326	0.017	0.012
X(phase)	0.71	0.61	0.60	0.58	0.46	0.73	0.22	0.22	0.28	0.33	0.69	0.20	0.23	0.59	0.27	0.34
Y(phase)							0.28	0.20				0.27	0.21			

$X(Grt) = X_{Py} = Mg/(Fe^{2+}+Mg + Ca + Mn)$; $Y(Grt) = X_{Grs} = Ca/(Fe^{2+}+Mg + Ca + Mn)$; others are as in **Table 2**.

FIGURE 3 | Photomicrographs of sample JD15120. **(A,B)** Coexistence of medium-grained Cpx-1, Opx-1, Pl-1, Amp-1, and ilmenite. **(C,D)** Vermicular minerals of Cpx-2, Opx-2, Amp-2, Pl-2, and quartz along the margin of Amp-1 and Pl-1.
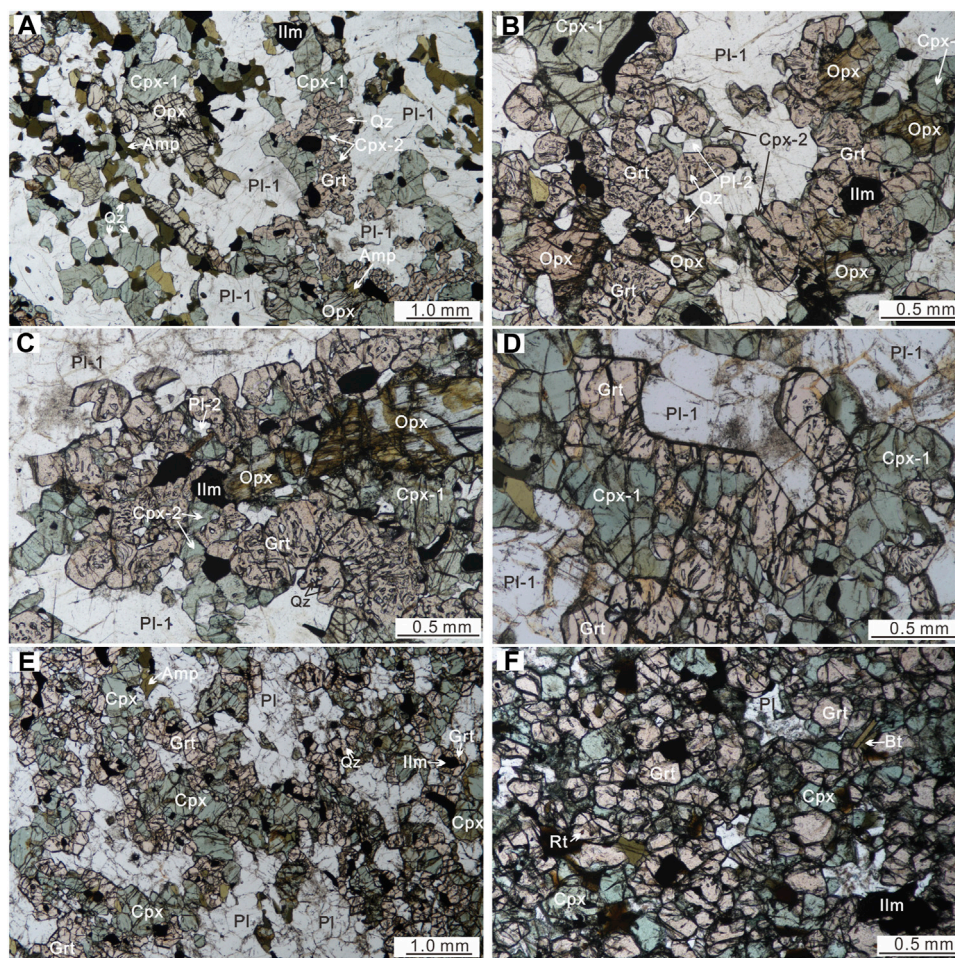
FIGURE 4 | Photomicrographs of samples YC8-43 and JD1546: **(A)** Large-scale photograph showing mineral relations that medium-grained orthopyroxene, Cpx-1, Pl-1, and amphibole are overprinted by fine-grained garnet, Cpx-2, Pl-2, and quartz in YC8-43; **(B,C)** poikilitic garnet with worm-like quartz inclusions occurring with fine-grained Cpx-2 and Pl-2 around medium-grained Cpx-1 and orthopyroxene in YC8-43; **(D)** garnet occurring as "red-eye pocket" separating Cpx-1 from Pl-1 in YC8-43; and **(E,F)** photomicrographs of the sample JD1546 showing the coexistence of fine-grained garnet, clinopyroxene, amphibole, and plagioclase with minor amounts of quartz and biotite.

beam diameter of 2 μm. Natural and synthetic minerals of the SPI Company were used for standardization. Representative mineral analyses are listed in **Tables 2**, **3**. Photomicrographs are shown in **Figures 3**, **4**.

Sample JD15120 is a two-pyroxene granulite with a weak foliation, comprising mostly clinopyroxene (25 vol%), orthopyroxene (15 vol%), amphibole (27 vol%), plagioclase (30 vol%), and minor amounts of biotite, quartz, and ilmenite. It shows overall equigranular texture, where the fine-to medium-grained (0.2–1.0 mm across) clinopyroxene, orthopyroxene, amphibole, and plagioclase directly contact with each other (hereafter Cpx-1, Opx-1, Amp-1, and Pl-1, respectively) (**Figures 3A,B**). Amp-1 can also occur surrounding or replacing clinopyroxene at rims, suggesting later growth (**Figure 3B**). Occasionally, there are vermiform minerals of <0.1 mm, including clinopyroxene, orthopyroxene, amphibole, and plagioclase (hereafter Cpx-2, Opx-2, Amp-2, and Pl-2 respectively), occurring as coronae around Amp-1 or along the

boundary between Amp-1 and Pl-1 (**Figures 3C,D**). Clinopyroxene (Cpx-1 and Cpx-2) shows similar diopsidic compositions with En [= Mg/(Ca + Mg + Fe^{2+})] of 0.36–0.39, Fs [= Fe^{2+}/(Ca + Mg + Fe^{2+})] of 0.12–0.16, Wo [= Ca/(Ca + Mg + Fe^{2+})] of 0.46–0.49, and X_{Mg} [= Mg/(Mg + Fe^{2+})] of 0.68–0.76 (Morimoto 1988), but Cpx-1 occasionally has exsolution lamellae of ilmenite in the core. Orthopyroxene (both Opx-1 and Opx-2) has composition of hypersthene with En of 0.52–0.57, Fs of 0.42–0.47, Wo of ~0.01, and X_{Mg} of 0.52–0.67 (Morimoto 1988). Amphibole (Amp-1 and Amp-2) has similar composition of pargasite involving K$_2$O of 1.45–1.82 wt%, Ca$_B$ = 1.76–1.89, (Na + K)$_A$ = 0.56–0.73, Si = 6.29–6.39, and X_{Mg} = 0.52–0.63 (Leake et al., 2003), but higher Ti of 0.18–0.28 p. f.u. in Amp-1 and lower Ti of 0.10–0.14 p. f.u. in Amp-2. Plagioclase commonly has cuspate boundaries. Pl-1 has chemical zonation with a constant X_{An} = Ca/(Ca + Na + K)] of 0.39–0.41 in the core but outward decreasing to 0.34–0.36 in the rim (**Figure 5A**), while Pl-2 shows slightly lower X_{An} of 0.35–0.39. A few biotite flakes
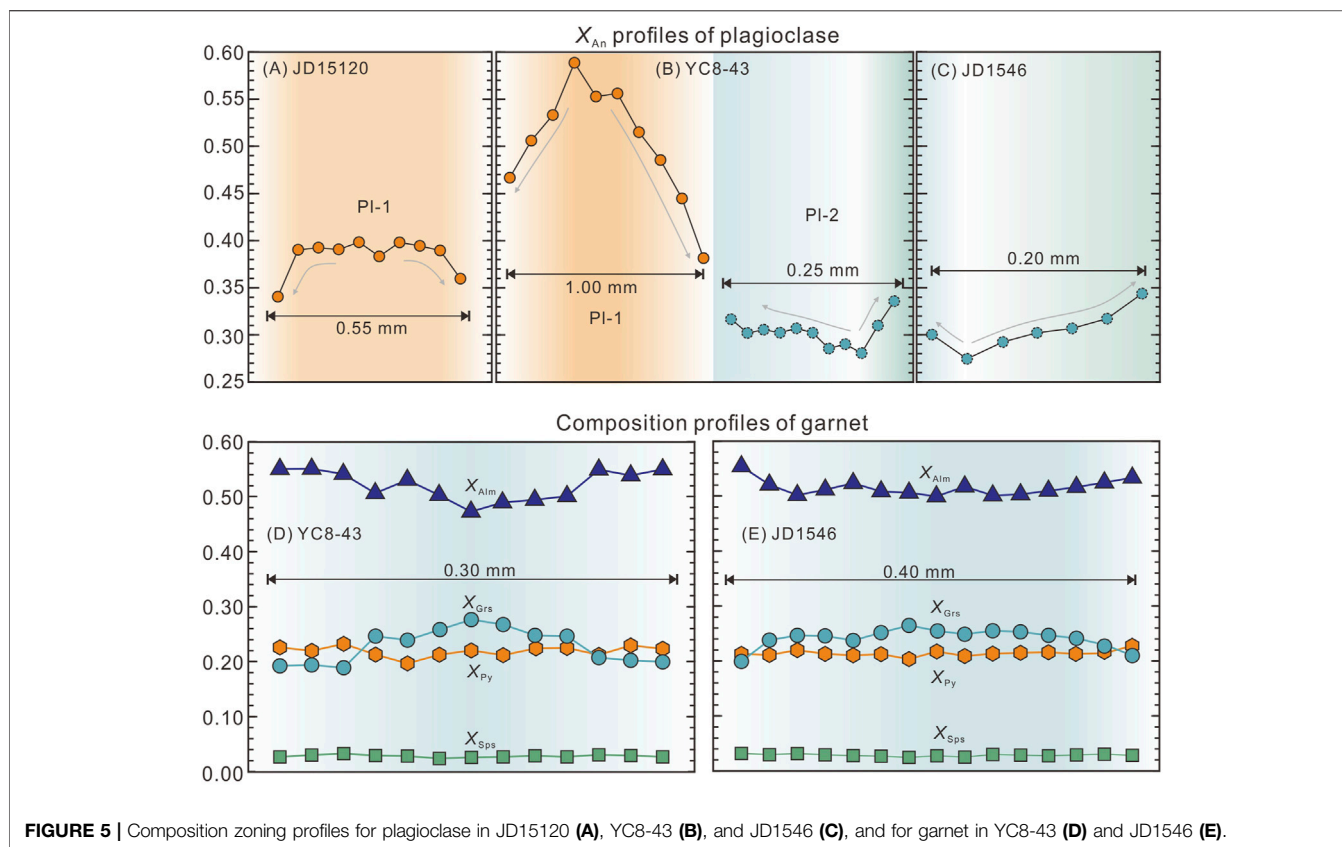
FIGURE 5 | Composition zoning profiles for plagioclase in JD15120 **(A)**, YC8-43 **(B)**, and JD1546 **(C)**, and for garnet in YC8-43 **(D)** and JD1546 **(E)**.

occur around Amp-1 or Cpx-1, suggesting their later growth. Additionally, ilmenite occurs as anhedral grains, and minor amounts of quartz exhibit as irregular shapes coexisting with the rim of Pl-1, or as vermiform grains in coronae. On the basis of the mineral relations and compositions, two generations of assemblage can be inferred for the sample. The first generation comprises the fine-to-medium-grained minerals that include the peak and final stages. The peak assemblage is featured with the coexistence of Cpx-1, Opx-1, Amp-1, Pl-1, and ilmenite, while the final assemblage is characterized by the re-growth of Amp-1 and Pl-1 and the emergence of biotite and quartz. The second generation of assemblage consists of the vermiform minerals of Cpx-2, Opx-2, Amp-2, Pl-2, and Qz in the coronae mostly around Amp-1.

Sample YC8-43 is a garnet-bearing two-pyroxene granulite, comprising clinopyroxene (20 vol%), orthopyroxene (17 vol%), garnet (15 vol%), amphibole (15 vol%), plagioclase (30 vol%), ilmenite (3 vol%), and minor amounts of quartz, biotite, and rutile (**Figures 4A–D**). Clinopyroxene occur either as subhedral to anhedral grains of 0.3–1.2 mm in contact with orthopyroxene (hereafter Cpx-1), or as irregular grains of <0.2 mm coexisting with garnet (hereafter Cpx-2). Both of the two types have similar diopsidic compositions with En of 0.36–0.38, Fs of 0.14–0.17, Wo of 0.46–0.48, and X_{Mg} of 0.67–0.73 (Morimoto 1988). Orthopyroxene shows as anhedral grains of 0.3–1.8 mm and has hypersthene compositions, containing En of 0.60–0.63, Fs of 0.37–0.39, Wo of ~0.01, and X_{Mg} of 0.61–0.63 (Morimoto

1988). Plagioclase is subdivided into tabular grains of 0.3–1.5 mm in diameter (Pl-1) or irregular grains of <0.3 mm (Pl-2). Pl-1 mostly contacts to Cpx-1, orthopyroxene and amphibole, but occasionally be separated from pyroxenes by garnet (**Figures 4C,D**). It exhibits core-to-rim zoning with X_{An} decreasing from 0.56 to 0.59 in the core to 0.38–0.47 in the rim (**Figure 5B**). Pl-2 occurs with garnet and Cpx-2, exhibiting core to rim zoning with increasing X_{An} from 0.28 to 0.34 (**Figure 5B**). Garnet is 0.2–0.5 mm poikilitic grains with numerous quartz inclusions (**Figures 4B–D**). It occurs alone or with Cpx-2 surrounding Cpx-1 and/or orthopyroxene, forming "red-eye socket" textures to separate Cpx-1 and orthopyroxene from Pl-1 (**Figures 4C,D**; Wei et al., 2014). It has almost constant X_{Py} [= Mg/(Ca + Mg + Fe^{2+}+Mn), defined accordingly for other components] mostly of 0.21–0.23 (with a maximum of 0.25) and X_{Sps} of ~0.03, but shows core-to-rim increasing X_{Alm} (0.48→0.56) and decreasing X_{Grs} (0.28→0.20) (**Figure 5D**). Amphibole is mostly anhedral grains with sizes of 0.2–0.8 mm directly contacting to pyroxenes, or irregular shapes surrounding Cpx-1, showing later growth. It has pargasite compositions (Leake et al., 2003) involving K$_2$O of 1.53–1.71 wt%, Ca$_B$ = 1.83–1.85, (Na + K)$_A$ = 0.60–0.73, Si = 6.21–6.37, Ti = 0.24–0.26 p. f.u. and X_{Mg} = 0.55–0.60 (Yang and Wei 2017a). Biotite occurs around amphibole, indicating their later growth. Ilmenite is irregular grains among minerals or as rounded grains within Cpx-1. It can also be included in garnet. Minor amounts of rutile occur as inclusions in garnet. Quartz occurs as interstitial grains among minerals, or as vermicular

inclusions in garnet. Based on petrological observations and mineral compositions, two generations of mineral assemblage can be inferred. The first generation is recognized to involve final and peak stages. The peak stage is marked by the coexistence of Cpx-1, orthopyroxene, Pl-1, amphibole, and ilmenite, while the final is featured with the growth of biotite and quartz. The second generation is characterized by the coexistence of poikilitic garnet, Cpx-2, Pl-2, quartz, and rutile.

Sample JD1546 is a garnet-clinopyroxene granulite, consisting of clinopyroxene (30 vol%), garnet (23 vol%), amphibole (17 vol%), plagioclase (28 vol%), ilmenite (2 vol%), and minor amounts of quartz and biotite (**Figures 4E,F**). The sample has an equigranular texture with grain sizes mostly of 0.1–0.5 mm, except for a few larger-sized clinopyroxene grains of 1.0–1.5 mm. Clinopyroxene has diopsidic compositions with En of 0.37–0.40, Fs of 0.12–0.17, Wo of 0.43–0.50, and X_{Mg} of 0.69–0.77 (Morimoto 1988). Plagioclase is anhedral, and exhibits core-to-rim zoning with increasing X_{An} from 0.27 to 0.35 (**Figure 5C**). Garnet occurs normally with clinopyroxene or as "red-eye socket" textures around clinopyroxene. It exhibits core-to-rim decreasing X_{Grs} of 0.27→0.21 and increasing X_{Alm} of 0.50→0.55, but contains almost constant X_{Py} of 0.20–0.23 and X_{Sps} of ~0.03 (**Figure 5E**). Amphibole is mostly irregular grains with cuspate boundaries, and has pargasite compositions with K_2O of 1.72–1.92 wt%, Ca_B = 1.78–1.83, $(Na + K)_A$ = 0.63–0.68, Si = 6.16–6.27, Ti = 0.20–0.23 p. f.u., and X_{Mg} of 0.59–0.63 (Leake et al., 2003). Minor amounts of biotite display as irregular flakes or sticks around amphibole or clinopyroxene, suggesting their later formation. Quartz mostly occurs as interstitial grains among other minerals. Ilmenite and rutile occur as irregular grains or as inclusions in garnet. Based on the aforementioned textural relations, the peak assemblage is inferred to involve clinopyroxene, garnet, amphibole, plagioclase, and rutile, and the later growth of amphibole and biotite may represent the post-peak evolution. Presence of the larger-sized clinopyroxene might represent the relicts from an earlier metamorphism.

4 METAMORPHIC *P–T* CONDITIONS

Pseudosection modeling for these samples was conducted using THERMOCALC 3.50 and the internally consistent thermodynamic dataset of Holland and Powell (2011) update (ds62) in the system NCKFMASHTO ($Na_2O–CaO–K_2O–FeO–MgO–Al_2O_3–SiO_2–H_2O–TiO_2–Fe_2O_3$). Mixing models are those presented for garnet, orthopyroxene, and biotite (White et al., 2014), melt, clinopyroxene, and amphibole (Green et al., 2016), plagioclase (Holland and Powell 2003), and ilmenite (White et al., 2000). Among these models, amphibole model "hb" and clinopyroxene model "aug" were used because they are suit for clinoamphibole including pargasite, and for high-temperature clinopyroxene, respectively. As JD15120 and JD1546 are overall homogeneous, the analyzed bulk-rock compositions were used for the phase equilibria modeling. Whereas for YC8-43, the first generation of assemblages was modeled using the analyzed composition, and the second generation of assemblages was calculated based on an
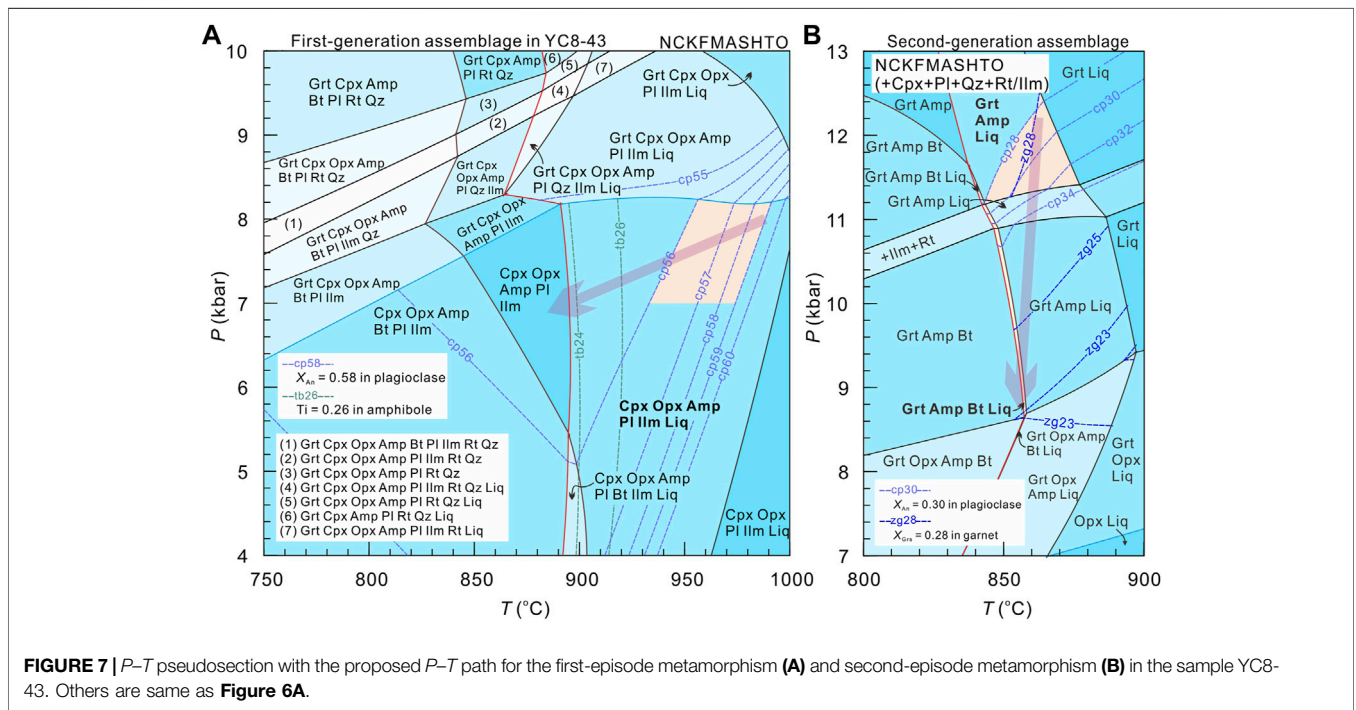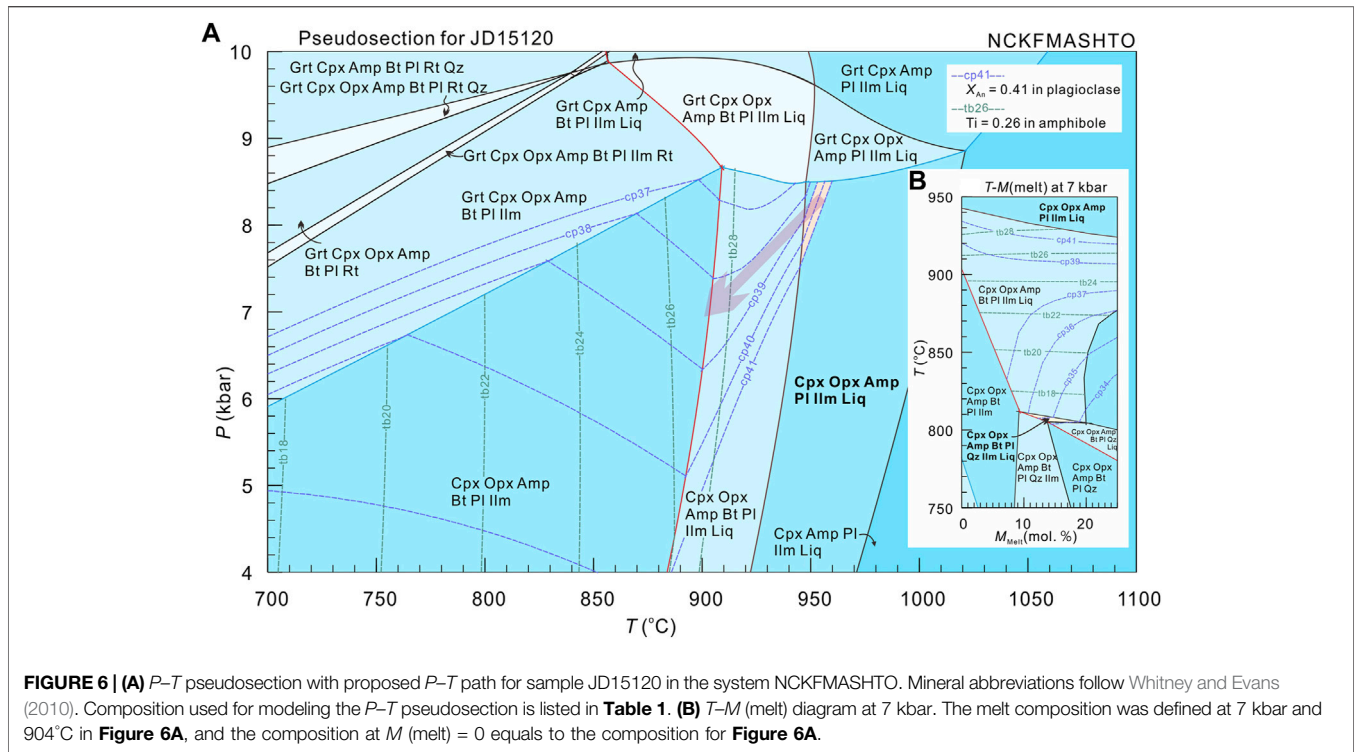
effective composition, generated on the basis of mass balance by integrating modal abundance and compositions of relevant minerals together (Carson et al., 1999). The H_2O contents and O (Fe_2O_3) values used in the modeling was defined using T–M (H_2O) and T–M(O) diagrams (e.g., Korhonen et al., 2011; Korhonen et al., 2012). Compositions used for modeling are presented in **Table 1**.

4.1 Sample JD15120
The *P–T* pseudosection for sample JD15120 was drawn within a *P–T* range of 4–10 kbar and 700–1,100°C (**Figure 6A**), contoured with isopleths of X_{An} in plagioclase and Ti in amphibole. The fluid-absent solidus occurs at temperatures of 830–900°C. The inferred peak assemblage involving medium-grained Cpx-1, Opx-1, Pl-1, Amph-1, and ilmenite is constrained under a large *P–T* condition of <8.5 kbar/900–1,010°C, limited by the garnet-in curve on the high-*P* limit, and biotite-in and orthopyroxene-out curves on the low- and high-*T* limits. The maximum X_{An} of 0.39–0.41 in the core of Pl-1 is plotted in the peak field and constrains a precise peak condition of 7.5–8.5 kbar/940–960°C with a temperature uncertainty of ~6°C (two-sigma level) calculated using THERMOCALC. It needs to be mentioned that this uncertainty should be considered as a minimum because it is propagated from the uncertainty on the enthalpy alone and does not include other sources of uncertainty. The post-peak decompressional cooling is driven by the reaction Cpx + Ilm + Liq = Opx + Pl + Amp + Bt, responsible for later growth of biotite and Amp-1, and also the outward decreasing X_{An} in Pl-1. The measured maximum Ti of 0.28 in Amp-1 is plotted in the biotite-present field, yielding temperatures of >910°C, whereas the lower Ti values were plotted in the sub-solidus fields. However, the observed final assemblage marked by the presence of quartz does not occur in **Figure 6A**, probably because the residual melts that produced the final assemblage were locally segregated and not completely equilibrated with other minerals. Therefore, we calculated a T–M (melt) pseudosection at 7 kbar by adding more melts in the final mineral assemblage on **Figure 6A**. As shown in **Figure 6B**, the fluid-absent solidus occurs at lower temperatures as the melt modes increase, and the quartz-present final assemblage appears at ~810°C on the solidus with the melt modes of 10–20 mol%. This field is well consistent with the measured X_{An} of 0.34–0.36 in the rim of Pl-1. Moreover, the measured lower Ti values in amphibole can also plot in the suprasolidus fields. Therefore, a post-peak decompressional cooling process from the peak condition of 7.5–8.5 kbar/940–960°C to the final condition of ~7 kbar/~810°C can be well constrained for JD15120.

4.2 Sample YC8-43
The *P–T* pseudosection for the first-generation of assemblages in YC8-43 was drawn within a *P–T* range of 4–10 kbar and 750–1,000°C (**Figure 7A**), contoured with isopleths of X_{An} in plagioclase and Ti in amphibole. The fluid-absent solidus occurs at temperatures of 860–890°C. The observed peak assemblage involving medium-grained Cpx-1, orthopyroxene, Pl-1, amphibole, and ilmenite is constrained under a large *P–T*

FIGURE 6 | (A) *P–T* pseudosection with proposed *P–T* path for sample JD15120 in the system NCKFMASHTO. Mineral abbreviations follow Whitney and Evans (2010). Composition used for modeling the *P–T* pseudosection is listed in **Table 1**. **(B)** *T–M* (melt) diagram at 7 kbar. The melt composition was defined at 7 kbar and 904°C in **Figure 6A**, and the composition at *M* (melt) = 0 equals to the composition for **Figure 6A**.

FIGURE 7 | *P–T* pseudosection with the proposed *P–T* path for the first-episode metamorphism **(A)** and second-episode metamorphism **(B)** in the sample YC8-43. Others are same as **Figure 6A**.

condition of <8 kbar/870–1,000°C, limited by the garnet-in curve on the high-*P* limit, and the liquid-out and amphibole-out curves on the low- and high-*T* limits. The measured maximum X_{An} of 0.59–0.56 in the core of Pl-1 is plotted in the peak assemblage field, and yields a peak temperature of 950–990°C at 8 kbar with
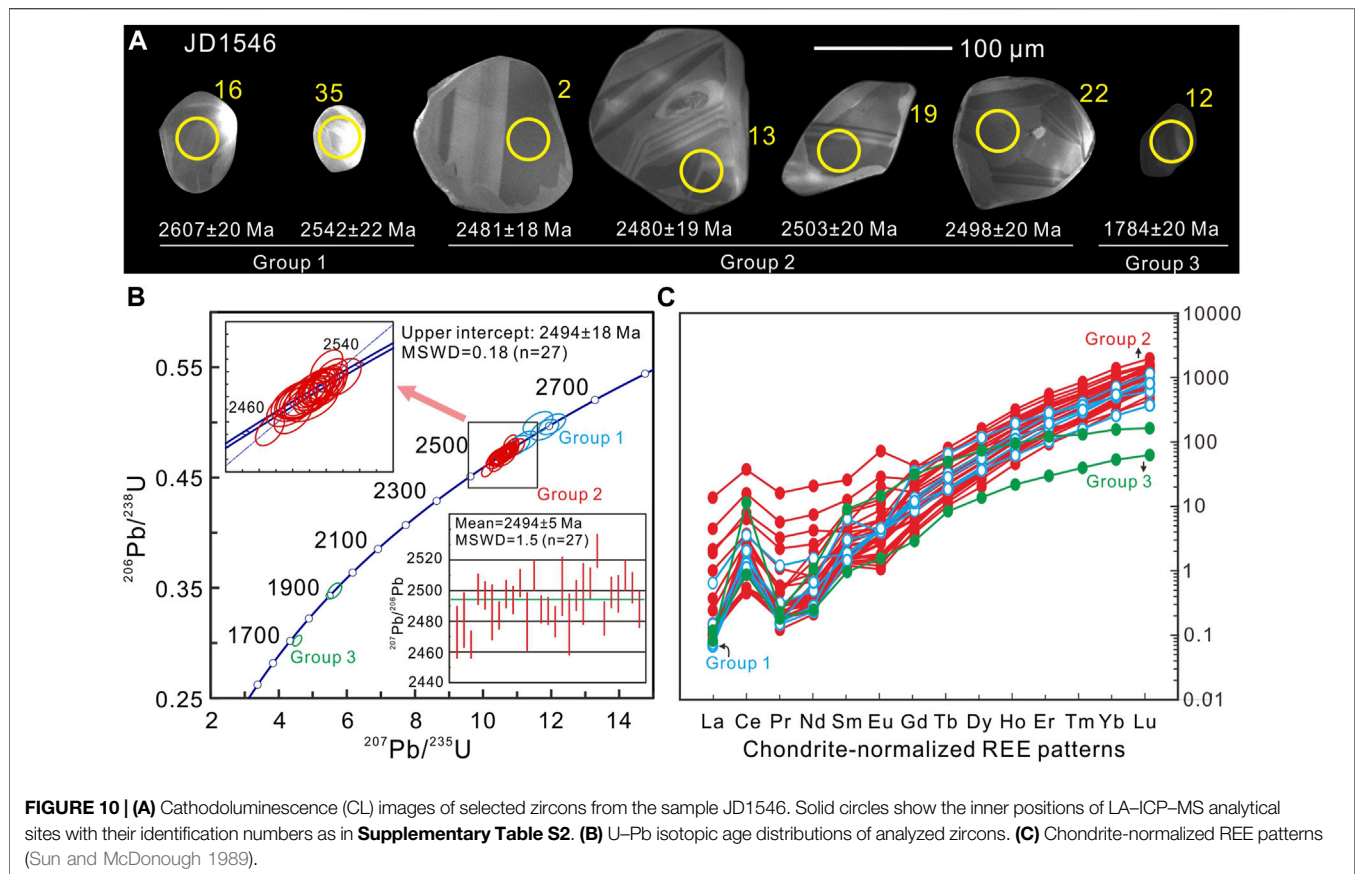
the uncertainty of ~6°C (two-sigma level). The post-peak decompression cooling is dominated by the reaction of Cpx + Ilm + Liq = Opx + Pl + Amp, being responsible for the observed re-growth of amphibole and the core-to-rim decreasing X_{An} in Pl-1. The measured Ti of 0.24–0.26 in amphibole is consistent with

FIGURE 8 | *P–T* pseudosection with the proposed *P–T* path for the sample JD1546. Others are same as **Figure 6A**.

the cooling evolution. Similar to JD15120, the quartz-present final assemblage and the measured X_{An} of 0.38–0.47 in the rim of Pl-1 do not occur in the pseudosection, as a result of local segregation of residual melts. This can be solved using an alternative pseudosection as in **Figure 6B**.

The second-generation of assemblages is modeled over a *P–T* range of 7–13 kbar and 800–900°C (**Figure 7B**), countered with the isopleths of X_{Grs} in garnet and X_{An} in plagioclase. The inferred peak assemblage including garnet, Cpx-2, Pl-2, amphibole, quartz, and rutile occurs within a large *P–T* of >11 kbar/810–880°C, constrained by the rutile-out curve in the low-*P* limit, and the liquid-out and amphibole-out curves in the low- and high-*T* limits. The measured maximum X_{Grs} of 0.28 in the garnet core and the minimum X_{An} of 0.28 in the Pl-2 core yield a precise peak condition of ~12 kbar/860°C within the peak assemblage field with uncertainties of ~1.6 kbar and ~22°C (two-sigma level). The post-peak decompression is dominated by the reaction of Grt + Cpx + Qz + Liq = Amp + Pl, responsible for the formation of outward increasing X_{An} in Pl-2 but decreasing X_{Grs} in garnet.

4.3 Sample JD1546

The *P–T* pseudosection for the sample JD1546 was calculated within a *P–T* range of 7–14 kbar and 750–950°C (**Figure 8**), contoured with isopleths of X_{Py} and X_{Grs} in garnet and X_{An} in plagioclase. The observed peak assemblage involving garnet, clinopyroxene, amphibole, plagioclase, and rutile is constrained under a *P–T* condition of >10.5 kbar/820–870°C, constrained by

the rutile-out curve on the low-*P* limit, and the K-feldspar-in and amphibole-out curves on the low- and high-*T* limits. The measured maximum X_{Grs} of 0.27 in the core of garnet and the minimum X_{An} of 0.27 in the core of plagioclase are plotted to yield a precise peak condition at ~12.6 kbar and ~835°C in the peak assemblage field with uncertainties of ~0.6 kbar and ~20°C (two-sigma level). This is almost consistent with the temperature defined by the measured maximum X_{Py} of 0.23 in garnet. The post-peak decompression is dominated by the reaction of Grt + Cpx + Qz + Liq = Amp + Pl ± Bt, in accordance with the outward increasing X_{An} in plagioclase but decreasing X_{Grs} in garnet, and also responsible for the later growth of amphibole and biotite.

5 ZIRCON DATING

Zircon grains from the samples JD15120 (two-pyroxene granulite) and JD1546 (garnet clinopyroxene granulite) were separated by conventional heavy liquid and magnetic separation followed by hand-picking under a binocular microscope. Selected grains were mounted in an epoxy resin, polished down to expose the grain centers, photographed in transmitted and reflected light, and imaged using cathode luminescence (CL). CL imaging was conducted at Peking University on a FEI PHILIPS XL30 SFEG SEM with 2-min scanning time under the condition of 15 kV and 120 μA. The zircon LA–ICP–MS U–Pb isotopic analyses were performed at Peking University using an Agilent 7500c ICP-MS system connected with a 193 nm ArF excimer laser system (COMPexPro 102) with the automatic positioning system. Zircon 91,500 was used as the standard and the standard silicate glass NIST was used to optimize the machine (Wiedenbeck et al., 1995; Wiedenbeck et al., 2004). The concentration of U, Th, and Pb elements were calibrated using ^{29}Si as an internal calibrant and NIST 610 as an external reference standard. ^{207}Pb/^{206}Pb, ^{206}Pb/^{238}U, and ^{207}Pb/^{235}U ratios and apparent ages were calculated using the GLITTER 4.4 (Van Achterbergh et al., 2001; Griffin 2008). The age calculations and plotting of concordia diagrams were carried out using ISOPLOT 3.0 (Ludwig 2003). Analyses described as "concordant" refer to <10% discordance. The results are presented in **Supplementary Tables S1, S2**.

Zircon grains in the sample JD15120 are mostly oval or round in shape and have sizes of 30–150 μm with length/width ratios of 1:1–2:1 (**Figure 9A**). Two groups can be recognized based on their appearances on CL images. Group-1 grains are mostly dim in their luminescence and have a sector, patchy, or fir-tree zones. Group-2 zircons have clear core–rim structures, where the grain cores show similar features with the group-1 zircons, and the rims, mostly 3–20 μm across, are gray in color and have structureless zones. We have conducted only 25 analyses on 25 group-1 grains or group-2 zircon cores, as the rims of group-2 zircons are much smaller than the diameter of the beam spot. The results yield apparent ^{207}Pb/^{206}Pb ages from 2529 ± 31 to 2447 ± 53 Ma. Most of the analyses were plotted on or close to the concordia curve in **Figure 9B** and define an upper intersect age of 2490 ± 19 Ma (MSWD = 0.21), with a weighted

FIGURE 9 | (A) Cathodoluminescence (CL) images of selected zircons from the sample JD15120. Solid circles show the inner positions of LA–ICP–MS analytical sites with their identification numbers as in **Supplementary Table S1. (B)** U–Pb isotopic age distributions of analyzed zircons. **(C)** Chondrite-normalized REE patterns (Sun and McDonough 1989).

mean age of 2488 ± 10 Ma (MSWD = 0.38). These zircons were analyzed to have the Th/U ratios of mostly 0.11–1.49, with only one outlier of 3.18. They show left inclined REE patterns with high $(Lu/Gd)_N$ of 25.97–100.00, and exhibit positive Ce anomalies (Ce/Ce* = 11.95–101.29), and mostly negative Eu anomalies (Eu/Eu* = 0.20–1.00) (**Figure 9C**). They are considered to grow from metamorphic melts (Rubatto 2002; Wan et al., 2011).

Zircons in the sample JD1546 are mostly rounded with size range within 20–150 μm and length/width ratios of 1:1–2:1 (**Figure 10A**). They can be subdivided into three groups based on their appearances on CL images. The group-1 zircons are mostly bright in their luminescence and have blurred oscillatory or sector zones. The group-2 accounts for the majority of zircons, and the grains are significantly coarse with sizes of mostly >80 μm and have clear core–rim structures. The grain cores are mostly dim in luminescence and have patchy or sector zones, while the rims are 5–30 μm wide with gray luminescence and structureless zones. The group-3 is rare and small with sizes of <40 μm, featured with dark or gray luminescence and structureless zones. Five analyses were obtained on five group-1 zircons with apparent [207]Pb/[206]Pb ages from 2522 ± 22 to 2607 ± 20 Ma (**Figure 10B**). These zircons show the Th/U ratios of 0.35–0.49 and exhibit left inclined REE patterns with $(Lu/Gd)_N$ of 17.24–32.22, positive Ce anomalies (Ce/Ce* = 9.95–17.33), and negative Eu anomalies (Eu/Eu* = 0.20–0.67) on the chondrite-

normalized REE patterns (**Figure 10C**). They are considered to be captured zircons of mafic magma. Twenty-seven analyses were conducted on 27 group-2 zircon cores and yielded apparent [207]Pb/[206]Pb ages ranging from 2465 ± 9 to 2526 ± 11 Ma. These results were plotted on or close to the concordia curve in **Figure 10B** and defined an upper intersect age of 2494 ± 18 Ma (MSWD = 0.18), with a weighted mean age of 2494 ± 5 Ma (MSWD = 1.5). These zircons have the Th/U ratios of mostly 0.24–0.38 with an outlier of 0.13. On the chondrite-normalized REE patterns, they display left inclined REE patterns with $(Lu/Gd)_N$ of 10.45–131.68, positive Ce anomalies (Ce/Ce* = 2.04–29.25), and positive or negative Eu anomalies (Eu/Eu* = 0.28–2.12) (**Figure 10C**). These zircons were considered to have a metamorphic origin (Corfu et al., 2003). The group-2 zircon rims are smaller than the beam diameter and cannot be analyzed. Only two analyses were obtained on two group-3 zircons. One grain (#12) has apparent [207]Pb/[206]Pb age of 1784 ± 20 Ma (**Figure 10B**). It has a low Th/U ratio of 0.07 than other zircons and displays significantly low total REE values, flat HREE pattern with $(Lu/Gd)_N$ of 21.34, positive Ce anomalies (Ce/Ce* = 5.77), and negative Eu anomalies (Eu/Eu* = 0.81) (**Figure 10C**). It is considered to be metamorphic zircons that coexist with garnet (Rubatto 2002). The other grain (#7) has an apparent [207]Pb/[206]Pb age of 1922 ± 26 Ma (**Figure 10B**) and the Th/U ratio of 0.30. As it has a flat HREE pattern situated between the REE patterns of group-2 zircon cores and #12 zircon

FIGURE 10 | (A) Cathodoluminescence (CL) images of selected zircons from the sample JD1546. Solid circles show the inner positions of LA–ICP–MS analytical sites with their identification numbers as in **Supplementary Table S2**. **(B)** U–Pb isotopic age distributions of analyzed zircons. **(C)** Chondrite-normalized REE patterns (Sun and McDonough 1989).

(**Figure 10C**); we considered that its result would be a mixture of two ages.

6 DISCUSSION

6.1 Metamorphic Evolution of Mafic Granulites

Based on the petrological observations and phase equilibria modeling, two-episode metamorphism can be referred from mafic granulites including the fist-episode UHT metamorphism and the later overprinting metamorphism.

6.1.1 The First-Episode Ultrahigh Temperature Metamorphism

The first-episode metamorphism is inferred in the samples JD15120 and YC8-43, suggesting a P–T path involving UHT peak conditions and post-peak decompressional cooling under normal granulite-facies conditions. The peak assemblage in both samples is inferred to consist of fine-to-medium-grained clinopyroxene, orthopyroxene, amphibole, plagioclase, and ilmenite. The peak conditions were constrained to be 940–960°C at 7.5–8.5 kbar for the sample JD15120 and 950–990°C at 8 kbar for the sample YC8-43, on the basis of the stability of the peak assemblages in P–T pseudosections and contours of the measured maximum X_{An} in the core of

plagioclase (**Figures 6A**, **7A**). The post-peak evolution is inferred to be dominated by cooling with decompression, which is supported by the later growth of amphibole and biotite, the measured core-to-rim decreasing X_{An} in plagioclase (**Figures 5A,B**), and the measured Ti in amphibole (**Figures 6A**, **7A**). For both of the samples, the observed quartz- and biotite-present final assemblages may represent local segregation of residual melts, and thus, record lower-temperature solidi (~810°C/7 kbar for JD15120 in **Figure 6B**) than those modeled in the P–T pseudosections in **Figures 6A**, **7A**. The peak UHT conditions are consistent with the REE-based geothermometric results of 948–1,031°C from Yang and Wei (2017a), which are much higher than conventional Cpx–Opx Fe–Mg exchange geothermometric results of 756–940°C (He and Ye 1992; Chen and Li 1996; Zhao et al., 1999; Yang and Wei 2017a). These suggest that both the X_{An} in plagioclase cores and REEs in pyroxenes have high potential for recording the peak temperatures for UHT granulites (Cherniak and Dimanov 2010; Liang et al., 2013; Li and Wei 2016). However, conventional Fe–Mg exchange geothermometers are most likely to record the closure of Fe–Mg diffusion between minerals, with temperatures even lower than the solidus recorded by the quartz-present final assemblages.

Similar UHT peak conditions with post-peak cooling and decompression processes to normal granulite-facies were recovered in mafic and pelitic or greywacke granulites from
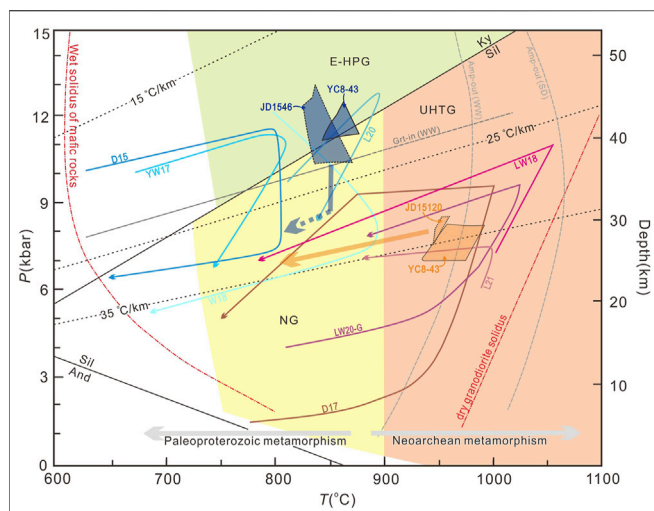
FIGURE 11 | Summarized $P–T$ conditions and paths for granulites from the East Hebei terrane. Thick arrows represent $P–T$ paths under peak $P–T$ conditions in this study. The $P–T$ paths from literatures are D15, from Duan et al. (2015); D17, from Duan et al. (2017); YW17, from Yang and Wei (2017a); W18, from Wang et al. (2018); LW18, from Liu and Wei (2018); LW20-G, path of meta-greywacke rock from Liu and Wei (2020); L20, from Lu and Wei (2020); and L21, from Liu et al. (2021). Mineral stabilities: Amp-out (WW) and Amp-out (SD) lines from the experiments of Wyllie and Wolf (1993) and Sen and Dunn (1994); Grt-in (WW) line is after Wyllie and Wolf (1993). The wet solidus of mafic rocks is after Lambert and Wyllie (1972) and the dry solidus of granodiorite is cited from Robertson and Wyllie (1971). The transition lines of Al_2SiO_5 are calculated by THERMOCALC. The abbreviations: NG—'normal' granulite; UHTG—ultrahigh-temperature granulite; EHPG—eclogite-high-pressure granulite.

the East Hebei terrane (Duan et al., 2017; Liu and Wei 2018; Liu and Wei 2020; Liu et al., 2021; **Figure 11**). In these granulites, pre-peak up-P processes can be inferred on the basis of 1) high-X_{An} plagioclase, spinel, or cordierite inclusions in garnet from pelitic granulites (Duan et al., 2017; Liu and Wei 2020; Liu et al., 2021), 2) orthopyroxene giving way to garnet in greywacke granulites (Liu and Wei 2020), and 3) rounded magnetite–ilmenite inclusions in clinopyroxene from mafic granulites (Liu and Wei 2018), suggesting anticlockwise $P–T$ paths (**Figure 11**).

6.1.2 The Overprinting Metamorphism
The overprinting metamorphism is recognized in all of the mafic granulites, but exhibits varying textures. In the sample JD15120 from the Taipingzhai ovoid-structural domain, the overprinting assemblages comprise tiny-grained clinopyroxene, orthopyroxene, plagioclase, amphibole, and quartz that occurred as vermicular coronae between medium-grained amphibole and plagioclase. In the sample YC8-43 from the central Saheqiao linear-structural belt, poikilitic garnet occurs as coronae or "red-eye sockets," or aggregates with tiny-grained clinopyroxene, plagioclase, amphibole, rutile, and quartz around the previous two-pyroxenes. Whereas in the sample JD1546 that from the west Saheqiao linear-structural belt, poikilitic garnet-bearing overprinting assemblages have completely replaced the previous UHT assemblages except for a few relics of medium-grained clinopyroxene. The garnet-bearing assemblages are

modeled to have peak $P–T$ conditions of ~12 kbar/860°C for YC8-43 and ~12.6 kbar/835°C for JD1546, based on the stability of the peak assemblages in the $P–T$ pseudosections, and the isopleths of the maximum X_{Grs} in garnet cores and the minimum X_{An} in plagioclase cores (**Figures 7B, 8**). The peak $P–T$ conditions are consistent with the results of 10–14 kbar/800–875°C calculated using REE- and major elements-based geothermobarometers (Yang and Wei 2017a). Similar HP granulite peak conditions of 9–11 kbar/~800°C and 12.5–12.8 kbar/880–900°C are also recovered in mafic granulites from the Malanyu and Beidazhangzi areas in the Saheqiao linear-structural belt (Wang et al., 2018; Lu and Wei 2020). Moreover, the overprinting assemblages in pelitic granulites from the Taipingzhai domain were also constrained to show peak conditions of 10–12 kbar/830–880°C, based on the high X_{Grs} of re-grown garnet (Duan et al., 2017). The post-peak decompression processes are inferred on the basis of the outward decreasing X_{Grs} in garnet and increasing X_{An} in plagioclase in this study and also in other supracrustal rocks (Lu and Wei 2020) and mafic dykes (Duan et al., 2015). In these research works, there are a few coarse-grained plagioclase grains recording a core-to-mantle decreasing X_{An} before the outward increasing X_{An} in the rim, being considered to suggest prograde up-T and P processes and clockwise $P–T$ paths (**Figure 11**).

6.2 Significance of Zircon Ages
Most metamorphic zircons from the samples JD15120 and JD1546 yielded ages of 2488 ± 10 Ma (MSWD = 0.38) and 2494 ± 5 Ma (MSWD = 1.5), respectively, which are considered to be related with the early-episode UHT metamorphism. This is because that 1) the zircons with the older ages are mostly large in size, round in shape, and have high Th/U ratios, showing the features of zircons that grew from metamorphic melts (Rubatto 2002; Wan et al., 2011); and 2) they display left-inclined REE patterns with high $(Lu/Gd)_N$ values, suggesting that no garnet was involved with the zircon growth (Rubatto 2002). These features are consistent with the recovered $P–T$ evolution of the early-episode UHT metamorphism. Moreover, the metamorphic ages are in accordance with the Neoarchean metamorphic ages of 2.55–2.46 Ga with a peak at ~2.50 Ga from supracrustal rocks in the East Hebei terrane (e.g., Nutman et al., 2011) and even in other terranes of the NCC (e.g., Huang et al., 2020).

Only one valid metamorphic age of 1784 ± 20 Ma was obtained from one zircon grain in the sample JD1546, which may correspond to the HP granulite-facies overprinting because that 1) the zircon is small in shape, dark in CL image, and has low Th/U ratio of 0.07, being consistent with zircons that from metamorphic fluid (Rubatto 2002; Wan et al., 2011); and 2) it displays the HREE-flat REE pattern with a low $(Lu/Gd)_N$ value, suggesting its equilibrium with garnet (Rubatto 2002). This age is consistent with the Lu–Hf garnet-whole rock isochron age of 1.77–1.79 Ga in similar granulites from the Saheqiao linear-structural belt (Yang and Wei 2017b). It is worthy to mention that the age of the HP granulite-facies overprinting had well dated to occur at 1.81–1.82 Ga from metabasic dykes (Duan et al., 2015) and other HP granulites (Yang and Wei 2017b; Lu and Wei 2020).

Note that although sample JD1546 is almost completely modified by HP granulite assemblages, its metamorphic zircons are mostly formed during the late Neoarchean UHT metamorphism. This suggests that zircons are more resistant than the major minerals during the lower-temperature overprinting on the higher-temperature UHT granulites. Therefore, it should be careful in linking the metamorphic assemblages with ages, especially for the rocks that have underwent multi-episode metamorphism.

6.3 Tectonic Implications

Two-episode metamorphism has been inferred in the East Hebei terrane, including the late Neoarchean UHT metamorphism and late Paleoproterozoic HP granulite-facies metamorphism, where the first one is featured with anticlockwise $P–T$ paths whereas the latter one is marked by clockwise $P–T$ paths (**Figure 11**). These two different metamorphic processes may suggest distinct tectonic settings.

6.3.1 Late Neoarchean Ultrahigh Temperature Metamorphism

The late Neoarchean UHT metamorphism in the East Hebei terrane may attribute from four tectonic models, including amalgamation of microcontinental terranes (e.g., Zhai and Santosh 2011), subduction–collision (e.g., Kusky et al., 2016; Liu et al., 2018), plume-related processes (e.g., Zhao et al., 1999; Geng et al., 2006), and vertical tectonics ("drip tectonics" or "sagduction"; e.g., Duan et al., 2017; Liu and Wei 2018,; Liu and Wei 2020). The Archean vertical tectonism is marked by mantle overturn and crustal delamination in the mantle–crust scale and sagduction within the crust (Johnson et al., 2014; Harris and Bédard 2014; Bédard 2018). A sagduction process, including the diapirism of granitoids and sinking of supracrustal rocks (e.g., Collins et al., 1998; Van Kranendonk et al., 2004), is considered to be the most possible mechanism that accounts for the formation of Archean unique dome–and–keel structures (e.g., Collins et al., 1998; Lin 2005; Lin and Beakhouse 2013; Parmenter et al., 2006), and the simultaneity between the metamorphism of supracrustal rocks and their ambient TTG magmatic activity (François et al., 2014). Thus, a sagduction process is preferred to be responsible for the late Neoarchean UHT metamorphism in the East Hebei terrane, based on the following lines of evidence: 1) the Archean unique dome–and–keel structures are well preserved (**Figure 1**), with the Lulong–Shuangshanzi supracrustal belt distributed between TTG domes and numerous supracrustal rafts within the domes; 2) the determined metamorphic ages of 2.55–2.46 Ga with a peak at ~2.50 Ga are coeval with the final pulse of TTG magmatism that ranging from 2.56 to 2.48 Ga with a peak at ~2.52 Ga (e.g., Wei 2018); and 3) near-vertical normal shear formed due to the upwelling of Anziling dome with respect to the down-slipping of the Lulong–Shuangshanzi supracrustal belt was inferred based on sub-vertical textures including mineral lineations and "S"-type folds in the Shuangshanzi shear zone (Liu et al., 2017; Zhao et al., 2021). The counterclockwise $P–T$ path in supracrustal rafts can be interpreted in a sagduction process, where the supracrustal rocks were heated first by the intrusion of high-temperature TTG magmas, or more possibly, the mantle-derived magmas, and

then dropped to magmas to reach the peak stage, and finally cooled and uplifted during the doming processes.

6.3.2 Late Paleoproterozoic Metamorphism

The late Paleoproterozoic metamorphism is widely observed in the NCC (e.g., Duan et al., 2015; Huang et al., 2016; Yang and Wei 2017b; Zou et al., 2022), and its tectonic setting has been controversially debated. The prevalent view suggests a successive collision model among the Archean blocks, forming the Khondalite belt at ~1.95 Ga, the Jiao-Liao-Ji belt at ~1.90 Ga, and the TNCO at ~1.85 Ga (e.g., Zhao et al., 2005; Zhao et al., 2012). However, the final amalgamation of the NCC along TNCO is argued to occur at ~1.95 Ga, and the dated age of ~1.85 Ga from granulites is interpreted to be correlated with a separated within-plate orogeny (Wei 2018; Qian et al., 2019). Another view contests that there were cold oceanic subduction and collision tectonics occurred in the north margin of the NCC (e.g., Kusky et al., 2016). The oceanic subduction is limited within 1.92–1.85 Ga and supported by the eclogite-facies metamorphism in the Chicheng ophiolitic mélange (Zhang Y. Y. et al., 2020; Zhang et al., 2021), and eclogite xenoliths with superdeep majorite inclusions in the carbonatite from the boundary between the Khondalite belt and TNCO (Xu et al., 2017; Xu et al., 2018), while the collision may occur later at 1.85–1.80 Ga with the similar spatial distribution of the IMNHO, between the NCC and a missing continent (Kusky et al., 2016) or the southwestern margin of the Siberia Craton (Wu et al., 2018).

In this study, late Paleoproterozoic metamorphism was well constrained in the East Hebei terrane, and it becomes weaker from north to south. In the Saheqiao linear-structural belt, HP granulite assemblages are well developed and stronger deformation had mostly removed the Neoarchean fabrics (Yang and Wei 2017a; Lu and Wei 2020; this article). In the Taipingzhai ovoid-structural domain, the Archean domal structures are survived, and the overprinting assemblages are limited in pelitic granulites with the regrowth of garnet (Duan et al., 2017), and in mafic granulites with the formation of vermicular coronae (**Figures 3C,D**), although good HP granulite assemblages are developed in mafic dykes (Duan et al., 2015). While in the Qian'an gneiss dome, overprinting assemblages were reported from the Caozhuang supracrustal rocks that are characterized by staurolite-bearing assemblages of low-amphibolite facies (Liu et al., 2020). Thus, the late Paleoproterozoic overprinting metamorphism in the East Hebei terrane suggests a medium P/T ratio at 1.78–1.82 Ga (Duan et al., 2015; Duan et al., 2017; Yang and Wei 2017b; Lu and Wei 2020; this article). This is considered to be correlated with intracontinental deformation that triggered by the oceanic subduction-related continental collision in the northern margin of the NCC. The collision event is also favored by the ~1.89 Ga Barrovian-type metamorphism in the Kondalite belt (Huang et al., 2016), the ~1.84 Ga HP granulites from the North Liaoning terrane (Duan et al., 2019), the 1.74–1.83 Ga amphibolite-to-granulite-facies metamorphism in the Miyun complex (He et al., 1993; Zhang H. C. G. et al., 2020; Zou et al., 2022), and the ~1.85 Ga within-plate metamorphism and deformation in the Wutai–Hengshan region (Wei 2018; Qian et al., 2019).

7 CONCLUSION

(1) Two-episode metamorphism can be recognized in mafic granulites from the East Hebei terrane.

(2) The first-episode metamorphism is recovered under UHT conditions of 940–990 °C at 7.5–8.5 kbar and post-peak cooling with the decompression process to ~7 kbar/~810 °C.

(3) The second-episode overprinting metamorphism exhibits varying textures in different samples. In garnet-bearing samples, the overprinting assemblages show HP granulite-facies peak conditions of 12–12.6 kbar/835–860°C, and post-peak isothermal decompression to ~9 kbar.

(4) Zircon dating suggests two metamorphic ages of ~2.49 Ga and ~1.78 Ga, being considered to be correlated with the UHT and HP granulite metamorphism, respectively.

(5) The late Neoarchean UHT granulite metamorphism with a thermal gradient of ~33°C/km may correlate a vertical sagduction regime, whereas the late Paleoproterozoic HP granulite metamorphism with a thermal gradient of ~20°C/km is favored to register the continental collision in the northern margin of the North China Craton.

DATA AVAILABILITY STATEMENT

The original contributions presented in the study are included in the article/**Supplementary Material**, further inquiries can be directed to the corresponding authors.

REFERENCES

AUTHOR CONTRIBUTIONS

TL calculated the pseudosections, performed the data analyses, and wrote the manuscript. CY and ZL collected the samples and conducted the experiments. CJW developed the project and revised the manuscript. All authors discussed the results and were involved in writing the paper.

SUPPLEMENTARY MATERIAL

The Supplementary Material for this article can be found online at: https://www.frontiersin.org/articles/10.3389/feart.2022.894353/full#supplementary-material

Arima, M., and Barnett, R. L. (1984). Sapphirine Bearing Granulites from the Sipiwesk Lake Area of the Late Archean Pikwitonei Granulite Terrain, Manitoba, Canada. *Contr. Mineral. Petrol.* 88, 102–112. doi:10.1007/BF00371415

Bai, X., Liu, S., Guo, R., and Wang, W. (2015). Zircon U-Pb-Hf Isotopes and Geochemistry of Two Contrasting Neoarchean Charnockitic Rock Series in Eastern Hebei, North China Craton: Implications for Petrogenesis and Tectonic Setting. *Precambrian Res.* 267, 72–93. doi:10.1016/j.precamres.2015.06.004

Bai, X., Liu, S., Guo, R., Zhang, L., and Wang, W. (2014). Zircon U-Pb-Hf Isotopes and Geochemistry of Neoarchean Dioritic-Trondhjemitic Gneisses, Eastern Hebei, North China Craton: Constraints on Petrogenesis and Tectonic Implications. *Precambrian Res.* 251, 1–20. doi:10.1016/j.precamres.2014.05.027

Bédard, J. H. (2018). Stagnant Lids and Mantle Overturns: Implications for Archaean Tectonics, Magmagenesis, Crustal Growth, Mantle Evolution, and the Start of Plate Tectonics. *Geosci. Front.* 9, 19–49. doi:10.1016/j.gsf.2017.01.005

Brown, M., and Johnson, T. (2018). Secular Change in Metamorphism and the Onset of Global Plate Tectonics. *Am. Mineral.* 103 (2), 181–196. doi:10.2138/am-2018-6166

Brown, M. (2007). Metamorphic Conditions in Orogenic Belts: A Record of Secular Change. *Int. Geol. Rev.* 49, 193–234. doi:10.2747/0020-6814.49.3.193

Carson, C. J., Powell, R., and Clarke, G. L. (1999). Calculated Mineral Equilibria for Eclogites in CaO-Na2O-FeO-MgO-Al2O3-SiO2-H2O: Application to the Pouébo Terrane, Pam Peninsula, New Caledonia. *J. Metamorph. Geol.* 17, 9–24. doi:10.1046/j.1525-1314.1999.00177.x

Chen, M. Y., and Li, S. X. (1996). The Evolution of Granulite Facies Metamorphism in Eastern Hebei Province. *Acta Petrol. Sin.* 12 (2), 343–357. (in Chinese with English abstract).

Chen, M. Y. (1990). Metabasic Dyke Swarms in a High-Grade Metamorphic Terrane: A Case Study in the Taipingzhai–Jinchangyu Area, Eastern Hebei Province. *Acta Geol. Sin.* 3, 427–441. (in Chinese with English abstract). doi:10.1111/j.1755-6724.1990.mp3004006.x

Cherniak, D. J., and Dimanov, A. (2010). Diffusion in Pyroxene, Mica and Amphibole. *Rev. Mineral. Geochem.* 72, 641–690. doi:10.2138/rmg.2010.72.14

Chu, H., Wang, H. C., Rong, G. L., Chang, Q. S., Kang, J. L., Jin, S., et al. (2016). The Geological Significance of the Rediscovered Fuchsite Quartzite with Abundant Eoarchean Detrital Zircons in Eastern Hebei Province. *Chin. Sci. Bull.* 61, 2299–2308. (in Chinese with English abstract). doi:10.1360/N972015-00998

Collins, W. J., Van Kranendonk, M. J., and Teyssier, C. (1998). Partial Convective Overturn of Archaean Crust in the East Pilbara Craton, Western Australia: Driving Mechanisms and Tectonic Implications. *J. Struct. Geology.* 20, 1405–1424. doi:10.1016/S0191-8141(98)00073-X

Corfu, F., Hanchar, J. M., Hoskin, P. W. O., and Kinny, P. (2003). Atlas of Zircon Textures. *Rev. Mineral. Geochem.* 53, 469–500. doi:10.2113/0530469

Duan, Z., Wei, C., and Qian, J. (2015). Metamorphic P–T Paths and Zircon U–Pb Age Data for the Paleoproterozoic Metabasic Dykes of High-Pressure Granulite Facies from Eastern Hebei, North China Craton. *Precambrian Res.* 271, 295–310. doi:10.1016/j.precamres.2015.10.015

Duan, Z., Wei, C. J., and Rehman, H. U. (2017). Metamorphic Evolution and Zircon Ages of Pelitic Granulites in Eastern Hebei, North China Craton: Insights into the Regional Archean P-T-T History. *Precambrian Res.* 292, 240–257. doi:10.1016/j.precamres.2017.02.008

Duan, Z. Z., Wei, C. J., and Li, Z. (2019). Metamorphic P-T Paths and Zircon U–Pb Ages of Paleoproterozoic Metabasic Dykes in Eastern Hebei and Northern Liaoning: Implications for the Tectonic Evolution of the North China Craton. *Precambrian Res.* 326, 124–141. doi:10.1016/j.precamres.2017.11.001

François, C., Philippot, P., Rey, P., and Rubatto, D. (2014). Burial and Exhumation during Archean Sagduction in the East Pilbara Granite-Greenstone Terrane. *Earth Planet. Sci. Lett.* 396, 235–251. doi:10.1016/j.epsl.2014.04.025

Frost, B. R., and Chacko, T. (1989). The Granulite Uncertainty Principle: Limitations on Thermobarometry in Granulites. *J. Geology.* 97, 435–450. doi:10.1086/629321

Fu, J., Liu, S., Chen, X., Bai, X., Guo, R., and Wang, W. (2016). Petrogenesis of Taxitic Dioritic-Tonalitic Gneisses and Neoarchean Crustal Growth in Eastern Hebei, North China Craton. *Precambrian Res.* 284, 64–87. doi:10.1016/j.precamres.2016.08.002

Geng, Y. S., Liu, F. L., and Yang, C. H. (2006). Magmatic Event at the End of the Archean in Eastern Hebei Province and its Geological Implication. *Acta Geol. Sin. (English Edition)* 80, 819–833. doi:10.1111/j.1755-6724.2006.tb00305.x

Green, E. C. R., White, R. W., Diener, J. F. A., Powell, R., Holland, T. J. B., and Palin, R. M. (2016). Activity-Composition Relations for the Calculation of Partial Melting Equilibria in Metabasic Rocks. *J. Metamorph. Geol.* 34, 845–869. doi:10.1111/jmg.12211

Griffin, W. L. (2008). Major Transformations Reveal Earth's Deep Secrets. *Geology* 36, 95–96. doi:10.1130/focus012008.1

Guo, R., Liu, S., Santosh, M., Li, Q., Bai, X., and Wang, W. (2013). Geochemistry, Zircon U-Pb Geochronology and Lu-Hf Isotopes of Metavolcanics from Eastern Hebei Reveal Neoarchean Subduction Tectonics in the North China Craton. *Gondwana Res.* 24, 664–686. doi:10.1016/j.gr.2012.12.025

Harley, S. L. (2004). Extending Our Understanding of Ultrahigh Temperature Crustal Metamorphism. *J. Mineral. Petrol. Sci.* 99, 140–158. doi:10.2465/jmps.99.140

Harley, S. L. (2008). Refining the P-T Records of UHT Crustal Metamorphism. *J. Metamorph. Geol.* 26, 125–154. doi:10.1111/j.1525-1314.2008.00765.x

Harley, S. L. (1989). The Origins of Granulites: A Metamorphic Perspective. *Geol. Mag.* 126, 215–247. doi:10.1017/s0016756800022330

Harley, S. L. (1998). Ultrahigh Temperature Granulite Metamorphism (1050 °C, 12 Kbar) and Decompression in Garnet (Mg70)-Orthopyroxene-Sillimanite Gneisses from the Rauer Group, East Antarctica. *J. Metamorph. Geol.* 16 (4), 541–562. doi:10.1111/j.1525-1314.1998.00155.x

Harris, L. B., and Bédard, J. H. (2014). "Interactions between Continent-Like 'Drift', Rifting, and Mantle Flow on Venus: Gravity Interpretations and Earth Analogues," in *Volcanism and Tectonism across the Solar System.* Editors T. Platz, M. Massironi, P. Byrne, and H. Hiesinger (London: Geological Society, Special Publication), 401.

He, G. P., and Ye, H. W. (1992). The Evolution of Metamorphism in Granulite Facies Terrane, Eastern Hebei Province. *Acta Petrol. Sin.* 8 (2), 129–135. (in Chinese with English abstract).

He, G. P., Ye, H. W., and Xia, S. L. (1993). Sm-Nd Isotopic Age of the Metamorphic Basic Dykes in Miyun, Beijing and its Geological Significance. *Acta Petrol. Sin.* 9, 312–317. (In Chinese with English abstract).

Holland, T. J. B., and Powell, R. (2011). An Improved and Extended Internally Consistent Thermodynamic Dataset for Phases of Petrological Interest, Involving a New Equation of State for Solids. *J. Metamorph. Geol.* 29, 333–383. doi:10.1111/j.1525-1314.2010.00923.x

Holland, T., and Powell, R. (2003). Activity-Composition Relations for Phases in Petrological Calculations: An Asymmetric Multicomponent Formulation. *Contrib. Mineral. Petrol.* 145, 492–501. doi:10.1007/s00410-003-0464-z

Huang, B., Kusky, T. M., Johnson, T. E., Wilde, S. A., Wang, L., Polat, A., et al. (2020). Paired Metamorphism in the Neoarchean: A Record of Accretionary-To-Collisional Orogenesis in the North China Craton. *Earth Planet. Sci. Lett.* 543, 116355. doi:10.1016/j.epsl.2020.116355

Huang, G., Jiao, S., Guo, J., Peng, P., Wang, D., and Liu, P. (2016). P-T-t Constraints of the Barrovian-Type Metamorphic Series in the Khondalite Belt of the North China Craton: Evidence from Phase Equilibria Modeling and Zircon U-Pb Geochronology. *Precambrian Res.* 283, 125–143. doi:10.1016/j.epsl.2020.11635510.1016/j.precamres.2016.07.011

Johnson, T. E., Brown, M., Kaus, B. J. P., and VanTongeren, J. A. (2014). Delamination and Recycling of Archaean Crust Caused by Gravitational Instabilities. *Nat. Geosci* 7, 47–52. doi:10.1038/ngeo2019

Jordan, T. H. (1978). Composition and Development of the Continental Tectosphere. *Nature* 274, 544–548. doi:10.1038/274544a0

Kelsey, D. E., and Hand, M. (2015). On Ultrahigh Temperature Crustal Metamorphism: Phase Equilibria, Trace Element Thermometry, Bulk Composition, Heat Sources, Timescales and Tectonic Settings. *Geosci. Front.* 6 (3), 311–356. doi:10.1016/j.gsf.2014.09.006

Korhonen, F. J., Powell, R., and Stout, J. H. (2012). Stability of Sapphirine + Quartz in the Oxidized Rocks of the Wilson Lake Terrane, Labrador: Calculated Equilibria in NCKFMASHTO. *J. Metamorph. Geol.* 30, 21–36. doi:10.1111/j.1525-1314.2011.00954.x

Korhonen, F. J., Saw, A. K., Clark, C., Brown, M., and Bhattacharya, S. (2011). New Constraints on UHT Metamorphism in the Eastern Ghats Province through the Application of Phase Equilibria Modelling and *In Situ* Geochronology. *Gondwana Res.* 20, 764–781. doi:10.1016/j.gr.2011.05.006

Kusky, T. M., Polat, A., Windley, B. F., Burke, K. C., Dewey, J. F., Kidd, W. S. F., et al. (2016). Insights into the Tectonic Evolution of the North China Craton through Comparative Tectonic Analysis: A Record of Outward Growth of Precambrian Continents. *Earth-Science Rev.* 162, 387–432. doi:10.1016/j.earscirev.2016.09.002

Kwan, L. C. J., Zhao, G., Yin, C., and Geng, H. (2016). Metamorphic P-T Path of Mafic Granulites from Eastern Hebei: Implications for the Neoarchean Tectonics of the Eastern Block, North China Craton. *Gondwana Res.* 37, 20–38. doi:10.1016/j.gr.2016.05.004

Lambert, I. B., and Wyllie, P. J. (1972). Melting of a Gabbro (Qtz Eclogite) with Excess H2O to 35 Kbars with Geological Applications. *J. Geol.* 80, 693–708. doi:10.1086/627795

Leake, B. E., Woolley, A. R., Birch, W. D., Burke, E. A. J., Ferraris, G., Grice, J. D., et al. (2003). Nomenclature of Amphiboles: Additions and Revisions to the International Mineralogical Association's 1997 Recommendations. *Can. Mineral.* 41, 1355–1362. doi:10.2113/gscanmin.41.6.1355

Li, X. W., and Wei, C. J. (2016). Phase Equilibria Modelling and Zircon Age Dating of Pelitic Granulites in Zhaojiayao, from the Jining Group of the Khondalite Belt, North China Craton. *J. Metamorph. Geol.* 34, 595–615. doi:10.1111/jmg.12195

Liang, Y., Sun, C., and Yao, L. (2013). A REE-In-Two-Pyroxene Thermometer for Mafic and Ultramafic Rocks. *Geochim. Cosmochim. Acta* 102, 246–260. doi:10.1016/j.gca.2012.10.035

Lin, S., and Beakhouse, G. P. (2013). Synchronous Vertical and Horizontal Tectonism at Late Stages of Archean Cratonization and Genesis of Hemlo Gold deposit, Superior Craton, Ontario, Canada. *Geology* 41, 359–362. doi:10.1130/G33887.1

Lin, S. (2005). Synchronous Vertical and Horizontal Tectonism in the Neoarchean: Kinematic Evidence from a Synclinal Keel in the Northwestern Superior Craton, Canada. *Precambrian Res.* 139, 181–194. doi:10.1016/j.precamres.2005.07.001

Liou, P., Guo, J., Huang, G., and Fan, W. (2017). 2.9 Ga Magmatism in Eastern Hebei, North China Craton. *Precambrian Res.* 326, 6–23. doi:10.1016/j.precamres.2017.11.002

Liu, B., Neubauer, F., Liu, J., Jin, W., Li, W., and Liang, C. (2017). Neoarchean Ductile Deformation of the Northeastern North China Craton: The Shuangshanzi Ductile Shear Zone in Qinglong, Eastern Hebei, North China. *J. Asian Earth Sci.* 139, 224–236. doi:10.1016/j.jseaes.2017.01.014

Liu, D. Y., Shen, Q. H., Zhang, Z. Q., Jahn, B. M., and Auvray, B. (1990). Archean Crustal Evolution in China: U–Pb Geochronology of the Qianxi Complex. *Precambrian Res.* 48, 226–244. doi:10.1016/0301-9268(90)90010-N

Liu, S. W., Wang, W., Bai, X., Guo, R. R., Fu, J. H., Guo, B. R., et al. (2018). Lithological Assemblages of Archean Meta-Igneous Rocks in Eastern Hebei-Western Liaoning Provinces of North China Craton, and Their Geodynamic Implications. *Earth Sci.* 43, 44–56. (in Chinese with English abstract). doi:10.3799/dqkx.2018.003

Liu, T., Wei, C. J., Kröner, A., Han, B. F., and Duan, Z. Z. (2020). Metamorphic P–T Paths for the Archean Caozhuang Supracrustal Sequence, Eastern Hebei Province, North China Craton: Implications for a Sagduction Regime. *Precambrian Res.* 340, 105346. doi:10.1016/j.precamres.2019.105346

Liu, T., Wei, C. J., Johnson, T. E., and Sizova, E. (2021). Newly-Discovered Ultra-High Temperature Granulites from the East Hebei Terrane, North China Craton. *Sci. Bull.* 67, 670–673. in press. doi:10.1016/j.scib.2021.12.023

Liu, T., and Wei, C. J. (2018). Metamorphic Evolution of Archean Ultrahigh-Temperature Mafic Granulites from the Western Margin of Qian'an Gneiss Dome, Eastern Hebei Province, North China Craton: Insights into the Archean Tectonic Regime. *Precambrian Res.* 318, 170–187. doi:10.1016/j.precamres.2018.10.007

Liu, T., and Wei, C. J. (2020). Metamorphic P–T Paths and Zircon U-Pb Ages of Archean Ultra-High Temperature Paragneisses from the Qian'an Gneiss Dome, East Hebei Terrane, North China Craton. *J. Metamorph. Geol.* 38, 329–356. doi:10.1111/jmg.12524

Liu, Z., and Yang, Z. (1994). The Tectonic Evolution of Archean High Grade Metamorphic Terrane, Eastern Hebei, China. *J. Changchun Univ. Earth Sci.* 24, 254–258. (in Chinese with English abstract).

Lu, H., and Wei, C. J. (2020). Late Neoarchean or Late Paleoproterozoic High-Pressure Granulite Facies Metamorphism from the East Hebei Terrane, North China Craton? *J. Asian Earth Sci.* 190, 104195. doi:10.1016/j.jseaes.2019.104195

Lu, J., Zhai, M.-G., Lu, L.-S., and Zhao, L. (2017). P-T-t Evolution of Neoarchaean to Paleoproterozoic Pelitic Granulites from the Jidong Terrane, Eastern North China Craton. *Precambrian Res.* 290, 1–15. doi:10.1016/j.precamres.2016.12.012

Ludwig, K. R. (2003). *User's Manual for Isoplot 3.00: A Geochronological Toolkit for Microsoft Excel (No. 4).* Berkeley: Berkeley Geochronology Center Special Publication No. 4.

Mahan, K. H., Goncalves, P., Flowers, R., Williams, M. L., and Hoffman-Setka, D. (2008). The Role of Heterogeneous Strain in the Development and Preservation of a Polymetamorphic Record in High-Pgranulites, Western Canadian Shield. *J. Metamorph. Geol.* 26, 669–694. doi:10.1111/j.1525-1314.2008.00783.x

Mezger, K., Bohlen, S. R., and Hanson, G. N. (1990). Metamorphic History of the Archean Pikwitonei Granulite Domain and the Cross Lake Subprovince, Superior Province, Manitoba, Canada. *J. Petrol.* 31, 483–517. doi:10.1093/petrology/31.2.483

Morimoto, N. (1988). Nomenclature of Pyroxenes. *Mineralogy Petrol.* 39, 55–76. doi:10.1007/bf01226262

Nutman, A. P., Wan, Y., Du, L., Friend, C. R. L., Dong, C., Xie, H., et al. (2011). Multistage Late Neoarchaean Crustal Evolution of the North China Craton, Eastern Hebei. *Precambrian Res.* 189, 43–65. doi:10.1016/j.precamres.2011.04.005

O'Brien, P. J., and Rotzler, J. (2003). High-Pressure Granulites: Formation, Recovery of Peak Conditions and Implications for Tectonics. *J. Metamorph. Geol.* 21 (1), 3–20. doi:10.1046/j.1525-1314.2003.00420.x

Parmenter, A. C., Lin, S., and Corkery, M. T. (2006). Structural Evolution of the Cross Lake Greenstone belt in the Northwestern Superior Province, Manitoba: Implications for Relationship between Vertical and Horizontal Tectonism. *Can. J. Earth Sci.* 43, 767–787. doi:10.1139/E06-006

Pattison, D. R. M., Chacko, T., Farquhar, J., and Mcfarlane, C. R. M. (2003). Temperatures of Granulite-Facies Metamorphism: Constraints from Experimental Phase Equilibria and Thermobarometry Corrected for Retrograde Exchange. *J. Geol.* 44, 867–900. doi:10.1093/petrology/44.5.867

Perchuk, L. L., van Reenen, D. D., Varlamov, D. A., van Kal, S. M., TabatabaeimaneshBoshoff, R., and Boshoff, R. (2008). P-T Record of Two High-Grade Metamorphic Events in the Central Zone of the Limpopo Complex, South Africa. *Lithos* 103, 70–105. doi:10.1016/j.lithos.2007.09.011

Polat, A., Kusky, T. M., Li, J. H., Fryer, B. J., Kusky, T., Li, J., et al. (2006). Geochemical and Petrological Evidence for a Suprasubduction Zone Origin of Neoarchean (Ca. 2.5 Ga) Peridotites, central Orogenic belt, North China Craton. *Geol. Soc. America Bull.* 118, 771–784. doi:10.1130/B25845.1

Qi, H. L., Hao, X. H., Zhang, X. D., and Nie, W. D. (1999). The Geological Features of Granite-Greenstone Belts in Qinglong River, Jidong. *Prog. Precambrian Res.* 22, 1–17. (in Chinese with English abstract).

Qian, J. H., and Wei, C. J. (2016). P-T-t Evolution of Garnet Amphibolites in the Wutai-Hengshan Area, North China Craton: Insights from Phase Equilibria and Geochronology. *J. Metamorph. Geol.* 34, 423–446. doi:10.1111/jmg.12186

Qian, J., Wei, C. J., Clarke, G. L., and Zhou, X. (2015). Metamorphic Evolution and Zircon Ages of Garnet-Orthoamphibole Rocks in Southern Hengshan, North China Craton: Insights into the Regional Paleoproterozoic P-T-T History. *Precambrian Res.* 256, 223–240. doi:10.1016/j.precamres.2014.11.013

Qian, J., Wei, C. J., Zhou, X., and Zhang, Y. (2013). Metamorphic P-T Paths and New Zircon U-Pb Age Data for Garnet-Mica Schist from the Wutai Group, North China Craton. *Precambrian Res.* 233, 282–296. doi:10.1016/j.precamres.2013.05.012

Qian, J., Yin, C., Wei, C. J., and Zhang, J. (2019). Two Phases of Paleoproterozoic Metamorphism in the Zhujiafang Ductile Shear Zone of the Hengshan

Complex: Insights into the Tectonic Evolution of the North China Craton. *Lithos* 330-331, 35–54. doi:10.1016/j.lithos.2019.02.001

Robertson, J. K., and Wyllie, P. J. (1971). Experimental Studies on Rocks from the Deboullie Stock, Northern Maine, Including Melting Relations in the Water-Deficient Environment. *J. Geology.* 79, 549–571. doi:10.1086/627675

Rubatto, D. (2002). Zircon Trace Element Geochemistry: Partitioning with Garnet and the Link between U-Pb Ages and Metamorphism. *Chem. Geology.* 184, 123–138. doi:10.1016/S0009-2541(01)00355-2

Sen, C., and Dunn, T. (1994). Dehydration Melting of a Basaltic Composition Amphibolite at 1.5 and 2.0 GPa: Implications for the Origin of Adakites. *Contr. Mineral. Petrol.* 117, 394–409. doi:10.1007/BF00307273

Song, S. G. (1990). Metamorphosed Basic and Ultrabasic Dyke Swarms in Taipingzhai Region, East Hebei. *J. Changchun Univ. Earth Sci.* 20, 421–428. (in Chinese with English abstract).

Sun, H., Xie, H. Q., Liu, S. J., Dong, C. Y., Liu, D. Y., and Wan, Y. S. (2016). Archean Magmatism and Metamorphism in the Huangbaiyu-Yangyashan Area, Eastern Hebei Province: Evidence from SHRIMP Zircon U–Pb Dating. *Geol. Bull.* 35, 27–42. (in Chinese with English abstract). doi:10.3969/j.issn.1671-2552.2016.01.004

Sun, S.-S., and McDonough, W. F. (1989). Chemical and Isotopic Systematics of Oceanic Basalts: Implications for Mantle Composition and Processes. *Geol. Soc. Lond. Spec. Publications* 42, 313–345. doi:10.1144/GSL.SP.1989.042.01.19

Van Achterbergh, E., Ryan, C., Jackson, S., and Griffin, W. L. (2001). *Data Reduction Software for LA-ICP-MS.* Ottawa: Mineralogical Society of Canada.

Van Kranendonk, M. J., Collins, W. J., Hickman, A., and Pawley, M. J. (2004). Critical Tests of Vertical vs. Horizontal Tectonic Models for the Archaean East Pilbara Granite-Greenstone Terrane, Pilbara Craton, Western Australia. *Precambrian Res.* 131, 173–211. doi:10.1016/j.precamres.2003.12.015

Wan, Y.-S., Liu, D.-Y., Dong, C.-Y., Xie, H.-Q., Kröner, A., Ma, M.-Z., et al. (2015). "Formation and Evolution of Archean Continental Crust of the North China Craton," in *Precambrian Geology of China*. Editor M Zhai (Berlin, Heidelberg: Springer), 59–136. doi:10.1007/978-3-662-47885-1_2

Wan, Y., Liu, D., Dong, C., Liu, S., Wang, S., and Yang, E. (2011). U-Th-Pb Behavior of Zircons under High-Grade Metamorphic Conditions: A Case Study of Zircon Dating of Meta-Diorite Near Qixia, Eastern Shandong. *Geosci. Front.* 2 (02), 137–146. doi:10.1016/j.gsf.2011.02.004

Wang, C., Song, S., Allen, M. B., Su, L., and Wei, C. J. (2018). High-Pressure Granulite from Jixian, Eastern Hebei, the North China Craton: Implications for Neoarchean to Early Paleoproterozoic Collision Tectonics. *Geol. Soc. Spec. Publ.* 478, 427–448. doi:10.1144/SP478.16

Wang, C., Song, S., Wei, C. J., Su, L., Allen, M. B., Niu, Y., et al. (2019). Palaeoarchaean Deep Mantle Heterogeneity Recorded by Enriched Plume Remnants. *Nat. Geosci.* 12, 672–678. doi:10.1038/s41561-019-0410-y

Weber, W. (1984). The Pikwitonei Granulite Domain: A Lower Crustal Level along the Churchill-Superior Boundary in central Manitoba" in Workshop on: A Cross Section of Archean Crust. LPI Tech. Rep. 83–03, 95–97.

Wei, C. (2018). Neoarchean Granulite Facies Metamorphism and its Tectonic Implications from the East Hebei Terrane. *Acta Petrol. Sin.* 34, 895–912. (in Chinese with English abstract).

Wei, C., Qian, J., and Zhou, X. (2014). Paleoproterozoic Crustal Evolution of the Hengshan-Wutai-Fuping Region, North China Craton. *Geosci. Front.* 5, 485–497. doi:10.1016/j.gsf.2014.02.008

White, R. W., Powell, R., Holland, T. J. B., Johnson, T. E., and Green, E. C. R. (2014). New Mineral Activity-Composition Relations for Thermodynamic Calculations in Metapelitic Systems. *J. Meta. Geol.* 32, 261–286. doi:10.1111/jmg.12071

White, R. W., Powell, R., Holland, T. J. B., and Worley, B. A. (2000). The Effect of TiO2 and Fe2O3 on Metapelitic Assemblages at Greenschist and Amphibolite Facies Conditions: Mineral Equilibria Calculations in the System K2O–FeO–MgO–Al2O3–SiO2–H2O–TiO2–Fe2O3. *J. Metamorph. Geol.* 18, 497–511. doi:10.1046/j.1525-1314.2000.00269.x

Whitney, D. L., and Evans, B. W. (2010). Abbreviations for Names of Rock-Forming Minerals. *Am. Mineral.* 95, 185–187. doi:10.2138/am.2010.3371

Wiedenbeck, M., Allé, P., Corfu, F., Griffin, W. L., Meier, M., Oberli, F., et al. (1995). Three Natural Zircon Standards for U-Th-Pb, Lu-Hf, Trace Element and Ree Analyses. *Geostandards Newsl.* 19, 1–23. doi:10.1111/j.1751-908X.1995.tb00147.x

Wiedenbeck, M., Hanchar, J. M., Peck, W. H., Sylvester, P., Valley, J., Whitehouse, M., et al. (2004). Further Characterisation of the 91500 Zircon Crystal. *Geostand Geoanalyt Res.* 28, 9–39. doi:10.1111/j.1751-908X.2004.tb01041.x

Wu, C., Zhou, Z., Zuza, A. V., Wang, G., Liu, C., and Jiang, T. (2018). A 1.9-Ga Mélange along the Northern Margin of the North China Craton: Implications for the Assembly of Columbia Supercontinent. *Tectonics* 37, 3610–3646. doi:10.1029/2018TC005103

Wu, J. S., Geng, Y. S., Shen, Q. H., Wan, Y. S., Liu, D. H., and Song, B. (1998). *Archean Geology Characteristics and Tectonic Evolution of Sino-Korea Paleo-Continent.* Beijing: Geological Publication House. (in Chinese).

Wu, J. S., and Geng, Y. S. (1991). *The Major Geological Events of the Early Precambrian in the North China Platform.* Beijing: Geological Publication House. (in Chinese).

Wyllie, P. J., and Wolf, M. B. (1993). Amphibolite Dehydration-Melting: Sorting Out the Solidus. *Geol. Soc. Lond. Spec. Publications* 76, 405–416. doi:10.1144/GSL.SP.1993.076.01.20

Xu, C., Kynický, J., Song, W., Tao, R., Lü, Z., Li, Y., et al. (2018). Cold Deep Subduction Recorded by Remnants of a Paleoproterozoic Carbonated Slab. *Nat. Commun.* 9, 2790. doi:10.1038/s41467-018-05140-5

Xu, C., Kynický, J., Tao, R., Liu, X., Zhang, L., Pohanka, M., et al. (2017). Recovery of an Oxidized Majorite Inclusion from Earth's Deep Asthenosphere. *Sci. Adv.* 3, e1601589. doi:10.1126/sciadv.1601589

Yang, C., and Wei, C. (2017b). Two Phases of Granulite Facies Metamorphism during the Neoarchean and Paleoproterozoic in the East Hebei, North China Craton: Records from Mafic Granulites. *Precambrian Res.* 301, 49–64. doi:10.1016/j.precamres.2017.09.005

Yang, C., and Wei, C. (2017a). Ultrahigh Temperature (UHT) Mafic Granulites in the East Hebei, North China Craton: Constraints from a Comparison between Temperatures Derived from REE-Based Thermometers and Major Element-Based Thermometers. *Gondwana Res.* 46, 156–169. doi:10.1016/j.gr.2017.02.017

Yang, J., Wu, F., Wilde, S., and Zhao, G. (2008). Petrogenesis and Geodynamics of Late Archean Magmatism in Eastern Hebei, Eastern North China Craton: Geochronological, Geochemical and Nd-Hf Isotopic Evidence. *Precambrian Res.* 167, 125–149. doi:10.1016/j.precamres.2008.07.004

Yang, Q.-Y., Santosh, M., Collins, A. S., and Teng, X.-M. (2016b). Microblock Amalgamation in the North China Craton: Evidence from Neoarchaean Magmatic Suite in the Western Margin of the Jiaoliao Block. *Gondwana Res.* 31, 96–123. doi:10.1016/j.gr.2015.04.002

Yang, Q.-Y., Santosh, M., and Tsunogae, T. (2016a). High-Grade Metamorphism during Archean-Paleoproterozoic Transition Associated with Microblock Amalgamation in the North China Craton: Mineral Phase Equilibria and Zircon Geochronology. *Lithos* 263, 101–121. doi:10.1016/j.lithos.2015.11.018

Zhai, M.-G., and Santosh, M. (2011). The Early Precambrian Odyssey of the North China Craton: A Synoptic Overview. *Gondwana Res.* 20, 6–25. doi:10.1016/j.gr.2011.02.005

Zhang, H. C. G., Peng, T., Liu, J.-H., Wang, J., Chen, Y.-C., Zhang, Q. W. L., et al. (2020). New Geochronological Evidences of Late Neoarchean and Late Paleoproterozoic Tectono-Metamorphic Events in the Miyun Area, North China Craton. *Precambrian Res.* 345, 105774. doi:10.1016/j.precamres.2020.105774

Zhang, L., Zhai, M., Zhang, X., Xiang, P., Dai, Y., Wang, C., et al. (2012). Formation Age and Tectonic Setting of the Shirengou Neoarchean Banded Iron deposit in Eastern Hebei Province: Constraints from Geochemistry and SIMS Zircon U-Pb Dating. *Precambrian Res.* 222-223, 325–338. doi:10.1016/j.precamres.2011.09.007

Zhang, Y. Y., Wei, C. J., and Chu, H. (2021). Multi-Phase Metamorphism in the Northern Margin of the North China Craton: Records from Metapelite in the Hongqiyingzi Complex. *Gondwana Res.* 98, 289–308. doi:10.1016/j.gr.2021.06.012

Zhang, Y. Y., Wei, C. J., and Chu, H. (2020). Paleoproterozoic Oceanic Subduction in the North China Craton: Insights from the Metamorphic P-T-T Paths of the Chicheng Mélange in the Hongqiyingzi Complex. *Precambrian Res.* 342, 105671. doi:10.1016/j.precamres.2020.105671

Zhang, Y. X., Yan, H. Q., Wang, K. D., and Li, F. Y. (1980). Komatiites from the Qianxi Group in the Eastern Hebei Province, China. *J. Changchun Univ. Earth Sci.* 10, 1–8. (In Chinese with English abstract).

Zhao, C., Zhang, J., Zhao, G., Yin, C., Chen, G., Liu, J., et al. (2021). Kinematics and Structural Evolution of the Anziling Dome-And-Keel Architecture in East China: Evidence of Neoarchean Vertical Tectonism in the North China Craton. *Geol. Soc. Am. Bull.* in press. doi:10.1130/B36225.1

Zhao, G., Cawood, P. A., Li, S., Wilde, S. A., Sun, M., Zhang, J., et al. (2012). Amalgamation of the North China Craton: Key Issues and Discussion. *Precambrian Res.* 222-223, 55–76. doi:10.1016/j.precamres.2012.09.016

Zhao, G., Sun, M., Wilde, S. A., and Sanzhong, L. (2005). Late Archean to Paleoproterozoic Evolution of the North China Craton: Key Issues Revisited. *Precambrian Res.* 136, 177–202. doi:10.1016/j.precamres.2004.10.002

Zhao, G., Wilde, S. A., Cawood, P. A., and Lu, L. (1998). Thermal Evolution of Archean Basement Rocks from the Eastern Part of the North China Craton and its Bearing on Tectonic Setting. *Int. Geol. Rev.* 40, 706–721. doi:10.1080/00206819809465233

Zhao, G., Wilde, S. A., Cawood, P. A., and Lu, L. (1999). Thermal Evolution of Two Textural Types of Mafic Granulites in the North China Craton: Evidence for Both Mantle Plume and Collisional Tectonics. *Geol. Mag.* 136 (3), 223–240. doi:10.1017/S001675689900254X

Zou, L., Guo, J.-H., Huang, G.-Y., Jiao, S.-J., Tian, Z.-H., and Liu, P.-H. (2022). The Effect of Bulk Rock Composition in Phase Equilibria Modelling: A Case Study of Mafic Granulites from the North China Craton. *Contrib. Mineral. Petrol.* 177, 22. doi:10.1007/s00410-022-01887-9